DEPARTMENT OF PHYSICS
UNIVERSITY OF JYVÄSKYLÄ
RESEARCH REPORT No. 3/2006

LIFETIMES OF INTRUDER STATES IN ^{186,188}Pb AND ^{194}Po

BY
TUOMAS GRAHN

Academic Dissertation
for the Degree of
Doctor of Philosophy

To be presented, by permission of the
Faculty of Mathematics and Natural Sciences
of the University of Jyväskylä,
for public examination in Auditorium FYS-1 of the
University of Jyväskylä on May 19, 2006
at 12 o'clock noon

Jyväskylä, Finland
May 2006

ISBN 978-951-39-3168-1
URN:ISBN:978-951-39-3168-1

Preface

The work presented in this thesis has been carried out at the Accelerator Laboratory of the Department of Physics of the University of Jyväskylä during the years 2002 - 2006. During this time I have had the privilege to be part of the Gamma/RITU research group and share its enthusiastic and strongly professional atmosphere. The inspiring spirit of this group have guided me to carry on the high quality research in the field of experimental nuclear physics for which the Accelerator Laboratory is known for.

I am grateful to my supervisor Professor Rauno Julin for his valuable comments and advice throughout these years. Contribution of Dr. Alfred Dewald and his group from the University of Köln for this work - invaluable help during the experiments and later in the data analysis - is highly acknowledged. Dr. Sakari Juutinen, Dr. Peter Jones, Dr. Paul Greenlees and Dr. Juha Uusitalo deserve also a word of thanks for fruitful discussions about the theoretical and technical aspects of experimental nuclear physics.

I wish also to thank my closest colleagues Dr. Janne Pakarinen, Dr. Ari-Pekka Leppänen and Mr. Markus Nyman who have been great persons to work with.

Financial support from the Graduate School in Particle and Nuclear Physics, Ellen and Artturi Nyyssönen foundation, Emil Aaltonen foundation, Magnus Ehrnrooth foundation and Finnish Academy of Sciences and Letters; Vilho, Yrjö and Kalle Väisälä foundation is gratefully acknowledged.

To my loving wife Kristina and my dearest son Aleksanteri.

Jyväskylä, May 2006

Tuomas Grahn

Abstract

In this present work, a plunger device has been combined with the JUROGAM Ge-detector array and the RITU gas-filled separator in order to perform lifetime measurements of nuclear excited states produced by fusion-evaporation reactions. This work was carried out at the Accelerator laboratory of the University of Jyväskylä. Lifetimes of prolate intruder states in ^{186}Pb and oblate intruder states in ^{194}Po have been determined by employing, for the first time, the recoil-decay tagging technique in recoil distance Doppler-shift lifetime measurements. In addition, lifetime measurements of prolate states in ^{188}Pb up to the $I^{\pi} = 8^{+}$ state were carried out using the recoil gating method. The $B(E2)$ values have been deduced from which deformation parameters $|\beta_2| = 0.29(5)$ and $|\beta_2| = 0.17(3)$ for the prolate and the oblate bands, respectively, have been extracted.

These pioneering experiments, combining tagging techniques with the recoil distance Doppler-shift method, have shed new light on the collectivity and deformation of the intruder bands involving proton excitations across the $Z = 82$ shell gap. These excitations of small numbers of particles over the shell gap lead to dramatic changes in the nuclear shape. The present study addresses the phenomenon of shape coexistence typical for the nuclei near $Z = 82$ and $N = 104$ and provides information about configuration mixing of intrinsic structures of the nuclei of interest. The results are compared to the available lifetime data for neutron-deficient Hg and Pt nuclei.

Contents

1 Introduction

The spectacular phenomenon of shape coexistence observed in nuclei close to the proton drip-line near the shell gap at $Z = 82$ and neutron mid-shell at $N = 104$ is an active field of study in nuclear spectroscopy. The theoretical description of shape coexistence has been driven largely by experimental results and consequently, several theoretical approaches have recently been developed. The subject of shape coexistence is closely intertwined with the nuclear collective motion and especially quadrupole collectivity at low spin in neutron mid-shell Pb and Po nuclei. By probing properties of excited states in Pb and Po nuclei near the neutron mid-shell, information about the microscopic origin of shape coexistence and quadrupole collectivity can be extracted.

The shape of a finite many-body quantum system, such as the atomic nucleus, is not a quantum mechanical observable. This means that one cannot define an operator corresponding to the classical physical observable that is understood as a shape. The nearest which can be done is to measure the expectation values of the electromagnetic moments of a nuclear state, usually the quadrupole moment Q. It has been common practise to base shape coexistence arguments on the observed level spacings of band-members and if available, on electromagnetic transition probabilities. Indeed, the moment of inertia extracted from the level energies of the observed collective bands has in general a larger value for prolate states than that of oblate shapes (see e.g. Ref. [Juli 01]) and can provide qualitative information about the shape of the nucleus. However, the moment of inertia is not an absolute measure of collectivity or deformation as it can be influenced by other factors. Transition probabilities, in turn, extracted from level lifetimes offer a sensitive measure of collectivity

The unique case of ^{186}Pb, with well established triple shape coexistence [Andr 99a], offers a great laboratory to probe the electromagnetic properties of the prolate yrast band by employing the Recoil-Decay Tagging (RDT) method. While the proposed oblate band in ^{186}Pb is non-yrast [Paka 05b] and therefore weakly populated by fusion-evaporation reactions, an oblate yrast band has been observed in ^{192,194}Po. Probing electromagnetic properties of the oblate yrast band in ^{194}Po complements the present study of two different shapes by means of Recoil Distance Doppler-shift (RDDS) measurements in neutron-deficient Po and Pb region.

Due to their sensitivity to the details of the nuclear wave function, the knowledge of absolute transition probabilities and hence of lifetimes of nuclear levels are of special interest for our understanding of nuclear structure. Therefore, several methods to mea-

sure lifetimes have been developed. The methods most relevant to the sub-nanosecond time scale are the electronic timing method, the Doppler Shift Attenuation Method (DSAM) and the RDDS method. In the electronic timing method the time difference between populating and depopulating γ-rays of the level of interest is measured. This method is not applicable with the existing γ-ray detection sensitivity to nuclei with low production cross sections, such as the ones in the scope of this work. The DSAM is based on the measurement of a lineshape of γ-rays emitted by ions slowing down in matter. This technique requires a backed target where the recoils of interest eventually stop. This method is inapplicable for the neutron-deficient Pb and Po nuclei since it is necessary to use a recoil separator to select the reaction channel of interest. As the mechanism of Coulomb excitation is well understood, the measurement of the cross section of Coulomb excitation can also provide lifetime information. This method is also inapplicable for the nuclei studied in this work since such exotic beams as ^{186,188}Pb and ^{194}Po are not available in the present radioactive nuclear beam facilities. An excellent, if albeit slightly outdated review of techniques to measure a wide range of lifetimes of nuclear levels is given in Ref. [Nola 79].

In the present thesis a brief introduction to the theoretical background is given in Chapter 2. The experimental procedure is described in Chapter 3 and the results and their interpretations are given in Chapter 4. Chapter 5 summarises the present work.

In addition to acting as a spokesperson for the lifetime measurements presented in this work, the author has been responsible for the design, construction and operation of the JUROGAM Ge-detector array. The author has also given special attention to the maintenance and repair of the JUROGAM Ge-detectors. The results of the present work have also been reported in papers 1 and 2. The author has actively participated in other experimental studies carried out at the RITU recoil separator reported in papers 3 - 13. These studies cover an important part of the nuclear physics programme at the Department of Physics of the University of Jyväskylä.

1. **Collectivity and configuration mixing in ^{186,188}Pb and ^{194}Po**
   T. Grahn, A. Dewald, O. Möller, R. Julin, C. W. Beausang, I. G. Darby, S .Christen, S. Eeckhaudt, P. T. Greenlees, A. Görgen, K. Helariutta, J. Jolie, P. Jones, S. Juutinen, H. Kettunen, T. Kröll, R. Krücken, Y. Le Coz, M. Leino, A. -P. Leppänen, P. Maierbeck, D. A. Meyer, B. Melon, P. Nieminen, M. Nyman, R. Page, J. Pakarinen, P. Petkov, P. Rahkila, B. Saha, M. Sandzelius, J. Sarén, C. Scholey, J. Uusitalo, *Submitted to Physical Review Letters.*

2. **RDDS Lifetime Measurement with JUROGAM + RITU**
   T. Grahn, A. Dewald, O. Möller, C. W. Beausang, S. Eeckhaudt. P. T. Greenlees, J. Jolie, P. Jones, R. Julin, S. Juutinen, H. Kettunen, R. Krücken, T. Kröll, M. Leino, A.-P. Leppänen P. Maierbeck, D. A. Meyer, P. Nieminen, M. Nyman, J. Pakarinen, P. Petkov, P. Rahkila, B. Saha, C. Scholey, J, Uusitalo, *European*

Physical Journal A, Supplement 1, 441 (2005).

3. **Recoil-fission tagging of the transfermium nucleus ^{252}No**
A.-P. Leppänen, J. Uusitalo, P. T. Greenlees, R.-D. Herzberg, N. Amzal, F. Becker, P. A. Butler, A. J. C. Chewter, J. F. C. Cocks, O. Dorvaux, S. Eeckhaudt, K. Eskola, J. Gerl, T. Grahn, N. Hammond, K. Hauschild, K. Helariutta, F. P. Heßberger, M. Houry , G. D. Jones, P. M. Jones, R. Julin, S. Juutinen, H. Kankaanpää, H. Kettunen, T. L. Khoo, W. Korten, P. Kuusiniemi, Y. Le Coz, M. Leino, C. J. Lister, R. Lucas, M. Muikku, P. Nieminen, M. Nyman, R. Page, J. Pakarinen, P. Rahkila, P. Reiter, J. Sarén, Ch. Schlegel, C. Scholey, O. Stezowski, Ch. Theisen, W. H. Trzaska, H. J. Wollersheim, *Accepted for publication in European Physical Journal A.*

4. **Alpha-Decay Studies of the Nuclides ^{218}U and ^{219}U**
A. -P. Leppänen, J. Uusitalo, M. Leino, T. Grahn, P. T. Greenlees, P. Jones, R. Julin, S. Juutinen, H. Kettunen, P. Kuusiniemi, P. Nieminen, M. Nyman, J. Pakarinen, P. Rahkila, J. Sarén, C. Scholey, J. Sorri, G. Sletten, *To be submitted to Physical Review C.*

5. **First observation of a rotational band in the odd-Z transfermium nucleus $^{251}_{101}$Md**
A. Chatillon, Ch. Theisen, P. Bonche, E. Bouchez, P. Butler, E. Clément, O. Dorvaux, S. Eeckhaudt, B. J. P. Gall, A. Görgen, T. Grahn, P. T. G. Greenlees, P.-H. Heenen, R.-D. Herzberg, F. Heßberger, G. D. Jones, P. Jones, R. Julin, S. Juutinen, H. Kettunen, F. Khalfallah, W. Korten, Y. Le Coz, M. Leino, A-P. Leppänen, P. Nieminen, J. Pakarinen, J. Perkowski, P. Rahkila, M. Rousseau, C. Scholey, J. Uusitalo, J. N. Wilson, *To be submitted to Physical Review Letters.*

6. **Evidence for non-yrast states in ^{254}No**
S. Eeckhaudt, P. T. Greenlees, N. Amzal, J. E. Bastin, E. Bouchez, P. A. Butler, A. Chatillon, K. Eskola, J. Gerl, T. Grahn, A. Görgen, R.-D. Herzberg, F. P. Hessberger, A.Hürstel, P. J. C. Ikin, G. D. Jones, P. Jones, R. Julin, S. Juutinen, H. Kettunen, T. L. Khoo, W. Korten, P. Kuusiniemi, Y. Le Coz, M. Leino, A.-P. Leppänen, P. Nieminen, J. Pakarinen, J. Perkowski, A. Pritchard, P. Reiter, P. Rahkila, C. Scholey, Ch. Theisen, J. Uusitalo, K. Van de Vel, J. Wilson, *European Physical Journal A 26, 227 (2005).*

7. **Evidence for oblate structure in ^{186}Pb**
J. Pakarinen, I. G. Darby, S. Eeckhaudt, T. Enqvist, T. Grahn, P. T. Greenlees, V. Hellemans, F. Johnston-Theasby, P. Jones, R. Julin, S. Juutinen, H. Kettunen, M. Leino, A.-P. Leppänen, P. Nieminen, M. Nyman, R. D. Page, P. M. Raddon, P. Rahkila, C. Scholey, J. Uusitalo, R. Wadsworth, *Physical Review C 72, 011304(R) (2005).*

8. **α-decay studies of very neutron-deficient francium and radium isotopes**
   7.J. Uusitalo, M. Leino, T. Enqvist, K. Eskola, T. Grahn, P. T. Greenlees, P. Jones, R. Julin, S. Juutinen, A. Keenan, H. Kettunen, H. Koivisto, P. Kuusiniemi, A.-P. Leppänen, P. Nieminen, J. Pakarinen, P. Rahkila, C. Scholey, *Physical Review C 71, 024306 (2005).*

9. **First identification of γ-ray transitions in ^{107}Te**
   B. Hadinia, B. Cederwall, K. Lagergren, J. Blomqvist, T. Bäck, S. Eeckhaudt, T. Grahn, P. Greenlees, A. Johnson, D. T. Joss, R. Julin, S. Juutinen, H. Kettunen, M. Leino, A.-P. Leppänen, R. J. Liotta, P. Nieminen, M. Nyman, J. Pakarinen, E. S. Paul, P. Rahkila , C. Scholey, J. Uusitalo, R. Wadsworth, D. R. Wiseman, *Physical Review C 70, 064314 (2004).*

10. **Recoil decay tagging of γ rays in the extremely neutron-deficient nucleus ^{162}Os**
    D. T. Joss, K. Lagergren, D. E. Appelbe, C. J. Barton, J. Simpson, B. Cederwall, B. Hadinia, R. Wyss, S. Eeckhaudt, T. Grahn, P. T. Greenlees, P. M. Jones, R. Julin, S. Juutinen, H. Kettunen, M. Leino, A.-P. Leppänen, P. Nieminen, J. Pakarinen, P. Rahkila , C. Scholey, J. Uusitalo, R. D. Page, E. S. Paul, D. R. Wiseman, *Physical Review C 70, 017302 (2004).*

11. **Decay studies of ^{170,171}Au, $^{171-173}$Hg, and ^{176}Tl**
    H. Kettunen, T. Enqvist, T. Grahn, P. T. Greenlees, P. Jones, R. Julin, S. Juutinen, A. Keenan, P. Kuusiniemi, M. Leino, A.-P. Leppänen, P. Nieminen, J. Pakarinen, P. Rahkila , J. Uusitalo, *Physical Review C 69, 054323 (2004).*

12. **In-beam spectroscopy using the JYFL gas-filled magnetic recoil separator RITU**
    J. Uusitalo, P. Jones, P. Greenlees, P. Rahkila, M. Leino, A. N. Andreyev, P. A. Butler, T. Enqvist, K. Eskola, T. Grahn, R.-D. Herzberg, F. Hessberger, R. Julin, S. Juutinen, A. Keenan, H. Kettunen, P. Kuusiniemi, A-P. Leppänen, P. Nieminen, R. Page, J. Pakarinen, C. Scholey, The JUROSPHERE Collaboration, *Nuclear Instruments and Methods A 204, 638 (2003).*

13. **Alpha decay studies of the new isotopes ^{191}At and ^{193}At**
    H. Kettunen, T. Enqvist, T. Grahn, P. T. Greenlees, P. Jones, R. Julin, S. Juutinen, A. Keenan, P. Kuusiniemi, M. Leino, A.-P. Leppänen, P. Nieminen, J. Pakarinen, P. Rahkila , J. Uusitalo, *European Physical Journal A 17, 537 (2003).*

2 Physical background

2.1 Electromagnetic transitions and quadrupole moment

Most radioactive decays and nuclear reactions leave the residual nucleus in an excited state, which usually de-excites by an electromagnetic γ-ray transition. The γ-ray transition probability between the initial and final states with angular momenta I_i and I_f, respectively, is given by the formula

$$\lambda(L) = \frac{1}{\tau} = \frac{8\pi(L+1)}{\hbar L[(2L+1)!!]^2}\left(\frac{E_\gamma}{\hbar c}\right)^{2L+1} B(\mathcal{M}L; I_i \rightarrow I_f), \tag{2.1}$$

where τ is the mean lifetime of the state, $B(\mathcal{M}L; I_i \rightarrow I_f)$ is the reduced transition probability, E_γ is the energy difference between the initial and final states, L is the index of radiation defined so that 2^L is the multipole order ($L = 1$ for dipole, $L = 2$ for quadrupole and so on) and $\mathcal{M}$ indicates the character of the transition (E for electric and M for magnetic). The reduced transition probability is defined as

$$B(\mathcal{M}L; I_i \rightarrow I_f) = \frac{1}{2I_i+1}|\langle I_f||\hat{m}L||I_i\rangle|^2, \tag{2.2}$$

where $\hat{m}L$ is the electromagnetic multipole operator. Electromagnetic transitions obey the following angular momentum and parity π selection rules:

$$\begin{aligned} &|I_i - I_f| \leq L \leq I_i + I_f \quad \forall\, L \neq 0, \\ \Delta\pi = \text{no}: \quad &L = \text{even for electric}, L = \text{odd for magnetic}, \\ \Delta\pi = \text{yes}: \quad &L = \text{odd for electric}, L = \text{even for magnetic}. \end{aligned}$$

For the collective excitations in deformed nuclei the enhanced de-excitation mode is the electric quadrupole transition $E2$, especially the stretched $E2$ with $\Delta I = I_i - I_f$. Consequently all transitions investigated in this work are of stretched $E2$ character. For an $E2$ transition with $\Delta I = 2$ the reduced transition probability can be extracted from Eq. 2.1 and can be written as

$$B(E2) = \frac{0.0816}{E_\gamma^5(1+\alpha_{tot})\tau}\mathrm{e}^2\mathrm{b}^2, \tag{2.3}$$

where α_{tot} is the total internal conversion coefficient and τ given in units of ps including also the contribution of electron conversion and E_γ is given in units of MeV.

For an axially symmetric deformed rotating nucleus the reduced transition probability for the $I \rightarrow I-2$ $E2$-transitions within the rotational band can be written as (see e.g. [Bohr 75])

$$B(E2; KI_i \rightarrow KI_f) = \frac{5}{16\pi} e^2 Q_t^2 \langle I_f K 20 | I_i K \rangle^2, \tag{2.4}$$

where Q_t is the transition quadrupole moment. With the assumption of well behaving rotor the transitional quadrupole Q_t moment can be considered equal to the intrinsic quadrupole moment Q_0 which, in turn, is defined as

$$Q_0 = \sqrt{\frac{16\pi}{5}} \langle IK | E2 | IK \rangle. \tag{2.5}$$

As Eq. 2.2 indicates, the $B(E2)$ values are sensitive to the wave functions of the initial and final states. Since the electromagnetic operators are well known, the measurement of absolute transition probabilities reflects the details of nuclear wave functions and gives direct information about the structure of considered states. Equation 2.4 connects the $B(E2)$ value to the quadrupole moment of the transition, which is essentially the average of the intrinsic quadrupole moments of the initial and final states. If a large difference in intrinsic configurations occurs between the states I and $I-2$, i.e. the value of Q_t is low, the $B(E2)$ value will be significantly suppressed. Typical $B(E2)$ values for the collective transitions in deformed nuclei are of the order of 100 - 1000 Weisskopf units (W.u.), which is defined as an estimate for a single-particle transition probability.

2.2 Nuclear deformation

The shape of the axially symmetric deformed nucleus is described by the deformation parameter β_2, which represents the extent of quadrupole deformation and is related to the eccentricity of an ellipse as

$$\beta_2 = \frac{4}{3}\sqrt{\frac{\pi}{5}} \frac{\Delta R}{R_{ave}}, \tag{2.6}$$

where ΔR is the difference between semimajor and semiminor axes of the ellipse and the average of nuclear radius R_{ave} can be taken equal to $R_0 A^{1/3}$. By assuming a uniform charge distribution the intrinsic quadrupole moment is connected to β_2 by the formula

$$Q_0 = \frac{3}{\sqrt{5\pi}} Z R^2 \beta_2 (1 + 0.16\beta_2) e, \tag{2.7}$$

where Z is the atomic number and $R = R_0 A^{1/3}$ is the radius of the nucleus.

The quadrupole deformed nuclei are labelled as prolate ($Q_0 > 0$) or oblate ($Q_0 < 0$) having a form of an American football and a flat disk, respectively. From Eq. 2.7 one notes that Q_0 is directly proportional to β_2 in leading order.

The other important quantity to describe a quadrupole deformed nucleus is the moment of inertia $\mathcal{J}^{(1)}$, which is given as

$$\mathcal{J}^{(1)} = \frac{2}{5} M R^2 (1 + 0.31\beta_2), \tag{2.8}$$

where M is the mass of a nucleus. The moment of inertia given by Eq. 2.8 reduces to the familiar value of a sphere when $\beta_2 = 0$. It is notable that for the actual deformed nuclei ($\beta = 0 - 0.6$) the contribution of the deformation to the $\mathcal{J}^{(1)}$ is rather small. In the case of moderately deformed nuclei ($\beta_2 \approx 0.3$) this is only of the order of 10%.

In the hydrodynamical model the nucleus is considered to be an incompressible liquid droplet with a rigid core and its surface part rotating. The concept of irrotational flow takes place when the droplet is deformed having an axially symmetric shape. Then the hydrodynamical moment of inertia is given by the formula [Mori 76, Bohr 75]

$$\mathcal{J}^{(hydr)} = 3B\beta_2^2, \tag{2.9}$$

where B is the mass parameter as defined in Ref. [Bohr 75]. The moment of inertia is the result only of the eccentricity of the liquid droplet which is defined by β_2. A semi-empirical Grodzins formula [Grod 62] based on the global systematics of absolute transition probabilities from the first excited 2^+ state in even-even nuclei gives an estimate for the absolute transition probability

$$\lambda_\gamma(2^+ \to 0^+) = (3 \pm 1)10^{10}[E(2^+)]^4 Z^2 A^{-1}, \tag{2.10}$$

where E is the energy of the 2^+ state. This formula has been used to support the hydrodynamical relation (Eq. 2.9) and can be written as [Mori 76]

$$E(2^+) \approx \frac{1225}{A^{7/2}\beta_2^2} \text{ MeV}, \tag{2.11}$$

linking it to β_2 and furthermore to $\mathcal{J}^{(1)}$. Experimentally the kinematic moment of inertia for a quadrupole band derived from the rotational model can be extracted using the equation

$$\mathcal{J}^{(1)} = \frac{2I - 1}{E_\gamma}\hbar^2, \tag{2.12}$$

where I is the spin of the initial state and E_γ is the energy of the $I \to I - 2$ transition expressed in the units of MeV.

As given by Eq. 2.9 the moment of inertia is proportional to the square of the deformation parameter in the hydrodynamical model. This is in considerable contrast

to the kinematic moment of inertia given by the rotational model (see Eq. 2.8). As shown above, the moment of inertia does not only depend on the deformation but also has a strong dependence on the model itself. Therefore it cannot be used as a quantitative measure of deformation. An important problem in nuclear structure studies is to find the appropriate model to describe the structure of the nucleus of interest. The knowledge of transition probabilities offer a sensitive test for this purpose.

It is essential to note that Q_t is not directly measured, it is extracted from measured $B(E2)$ values. Since $B(E2)$ is a function of the square of Q_t as Eq. 2.4 indicates, in fact only the magnitude $|Q_t|$ is inferred. This means that one cannot distinguish between prolate and oblate shapes only by means of lifetime measurements. To resolve this ambiguity a more qualitative picture can be obtained by thoroughly studying the systematics of the energy levels and derived moments of inertia in the vicinity of the nucleus of interest. For instance, in the neutron-deficient even-mass Pb nuclei the association of the observed bands to the prolate shape has been based on the observed moments of inertia which are similar to those observed in neutron-deficient even-mass Hg and Pt nuclei [Juli 01]. In addition, the neutron deficient even-mass Po nuclei have a level pattern close to the ones of adjacent odd-mass nuclei. This can be seen as a decoupling of a neutron hole from an oblate core [Hela 99, Step 73] which, in turn, supports the picture of oblate shape of the yrast states in the vicinity of ^{194}Po.

2.3 Configuration mixing

When describing the structure of nuclear states, wave functions may be expressed in terms of any complete set of basis states spanning the Hilbert space. However, enormous simplification in calculations and greater physical meaning arises if a simple basis set is chosen. Often these basis states are associated with different coexisting intrinsic structures, which for the scope of this work are the previously mentioned spherical, oblate and prolate structures. It is of common interest to extract the amount of mixing between these shapes, i.e. the mixing amplitudes of the wave functions, from the experimental data. Since transition probabilities are very sensitive to the fine structure of wave functions they offer very beneficial information about configuration mixing in nuclei.

The reduced transition probability of an $E2$ transition can be expressed as

$$B(E2; I_i \rightarrow I_f) = \left[\sum_{jk} \alpha_j^i \alpha_k^f \langle j|E2|k\rangle \right]^2 , \tag{2.13}$$

where j, k denote the unperturbed states and the α_j^i and α_k^f are the corresponding orthonormal mixing amplitudes with $\sum_j \alpha_j^2 = 1$. Interpreting the previous formula in

a simple two-band mixing scheme where (a) the initial state i is assumed to be a pure deformed state with quadrupole moment Q_0^{def}, (b) the final state is assumed to be mixed and (c) interband transitions between unperturbed states are forbidden, then Eq. 2.13 reduces to

$$\sqrt{B(E2; I_i \rightarrow I_f)} = \alpha_j^f \sqrt{\frac{5}{16\pi}} \langle I_i^{def} K20 | I_f^{def} 0 \rangle Q_0^{def}. \tag{2.14}$$

In this relation Eq. 2.4 has been used and Q_t^{def} denotes the transition quadrupole moment of the pure deformed band. In the framework of this simple mixing scheme the mixing amplitudes of a given state can be extracted using measured electromagnetic properties of the states of interest.

Indeed, the two-band mixing scheme described above is the simplest one and is not applicable in general. More complex configuration mixing schemes have been developed and used to describe level structures and transition probabilities. Typical examples are given in references [Dewa 03, Drac 04] where the mixing calculations based on the experiments involving three coexisting bands in ^{188}Pb have been carried out and in Ref. [Hell 05] where the mixing calculations have been carried out for ^{188}Pb in the framework of interacting boson model.

2.4 Structure of neutron deficient even-even Pb and Po nuclei

In even-mass Pb nuclei, close to the neutron mid-shell at $N = 104$, deformed structures intrude down in energy close to the spherical ground state when approaching the neutron mid-shell. In the mid-shell nucleus ^{186}Pb the first two excited states are assigned as 0^+ states. Together with the spherical 0^+ ground state these levels establish a unique shape triplet for which $\pi(2p - 2h)$ and $\pi(4p - 4h)$ configurations can be inferred by α-decay studies [Andr 00]. Collective yrast bands, similar to those observed in neutron deficient even mass Hg and Pt isotopes [Juli 01], have also been observed in even mass isotopes $^{182-188}$Pb [Jenk 00, Cock 98, Baxt 93, Hees 93]. All these yrast bands have been experimentally associated with prolate shape. So far, candidates for collective non-yrast bands build on the coexisting oblate structures have been observed only in ^{186,188}Pb [Drac 04, Paka 05b].

In calculations based on a deformed mean-field [May 77, Naza 93] two rather close lying oblate and prolate minima appear next to the spherical ground state in the total energy surface and intrude down close to the ground state when approaching the neutron mid-shell. A similar picture is seen in recent Hartree-Fock-Bogoliubov (HFB) self-consistent configuration mixing calculations of mean-field states [Bend 04,

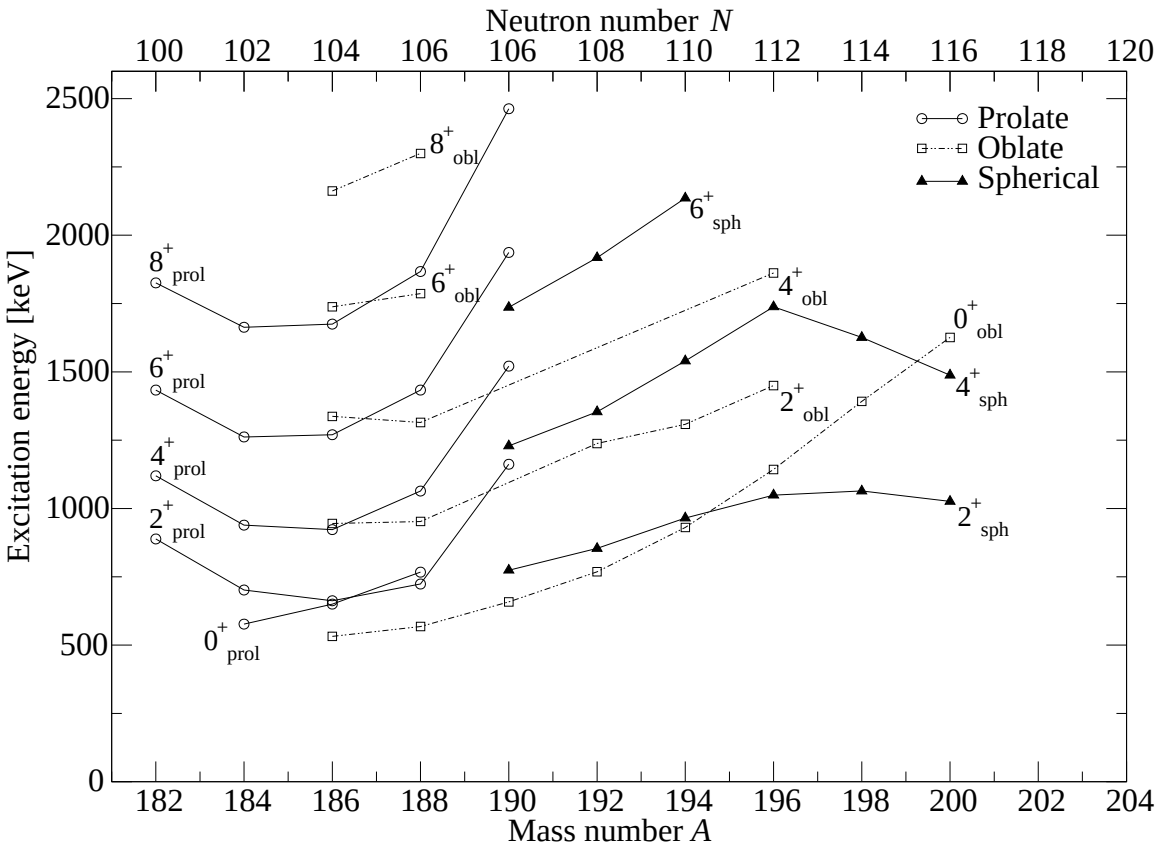

Figure 2.1: A selection of level systematics of the even-mass $^{182-200}$Pb isotopes. Data are taken from references [Jenk 00, Cock 98, Paka 05b, Drac 04, Sten 85, Alla 98, Drac 98, Van 87, Plom 93, Fant 91, Moor 95, Andr 00, Andr 99a, McDo 78, Penn 87] and references therein.

Rodr 04]. In the shell model language these coexisting structures are associated with $2p-2h$ and $4p-4h$ proton excitations across the $Z=82$ shell gap. The excitation energies are lowered by a residual quadrupole-quadrupole interaction and are predicted to be close to the $\pi(0p-0h)$ ground state near the neutron mid-shell [De C 00]. The mean-field oblate minimum can be associated with the proton $2p-2h$ excitation and the prolate one with the $4p-4h$ proton excitation [Naza 93].

Figure 2.1 shows a selection of levels in even-mass Pb isotopes as a function of mass number A. The energies of the levels associated with the oblate structure intrude down in energy with the decreasing neutron number so that the oblate 0^+ intruder state even becomes the first excited state below ^{194}Pb. The level energies of intruder structures reach their minimum at the neutron mid-shell $N=104$. The prolate intruder states have been seen in even-mass $^{182-190}$Pb isotopes while ^{186,188}Pb are the only lead nuclei where all the three coexisting 0^+ states have been observed [Andr 00, Alla 98] although the situation regarding the excited 0^+ states in ^{188}Pb is not clear [Van 03a]. The

yrast bands in ^{186,188}Pb are associated with rather pure prolate structure from spin 4^+ upwards whereas both experimental [Drac 04, Paka 05b] and theoretical [Hell 05] results suggest the strong mixing of 2^+ states.

Extending the spectroscopic studies to $Z = 84$, intruder structures have been verified in neutron-deficient Po isotopes. A sudden drop in level energies is observed in Po isotopes with $N \leq 114$, which is similar to that for the intruding 0_2^+ states observed in earlier α- and β-decay studies. These 0_2^+ states have been associated with proton $4p - 2h$ configurations [Bijn 95], and on the basis of Nilsson-Strutinsky calculations they are based on an oblate minimum [May 77]. Consequently, the observed yrast states in light even-mass Po isotopes down to ^{192}Po are presumed to form oblate bands. Based on the observed quadrupole vibrational features of ^{196,198}Po [Bern 95], the further suppression of level energies in ^{192,194}Po is alternatively explained as an evolution towards more collective anharmonic vibrator [Youn 95].

In Fig. 2.2, a systematics of low-lying levels in even-mass Po isotopes are illustrated. So far, non-yrast structures have only been seen in isotopes with $A \geq 194$. The level energy behaviour is rather smooth until at ^{198}Po a drop of energies of yrast states is observed [Bern 95, Maj 90, Albe 91, Hela 99]. In even-mass $^{192-196}$Po isotopes the yrast line forms a collective band built on the 0_2^+ state associated with the oblate $\pi(4p-2h)$ structure. In ^{194,196}Po levelling off of the yrast level energies is observed. In ^{190}Po, a band similar to the prolate bands in $^{182-188}$Pb has been observed [Van 03b] to cross the oblate ground state band at low spin. This is in accordance with theoretical predictions of prolate minimum reaching the ground state at ^{188}Po.

Configuration mixing of states associated with different shapes is predicted to be strong at low spin in the mid-shell Pb and Po region. Recently, lifetime measurements of excited states [Dewa 03] as well as spectroscopic studies [Drac 04] have established the strong mixing of the 2^+ state in ^{188}Pb. Dewald *et al.* [Dewa 03] have determined the squared prolate amplitude of 0.62 for the wave function of the yrast 2^+ state. The result is an outcome of a 3-band mixing analysis based on the measured level energies and fitted energies of unperturbed states. The result is consistent with the $B(E2; 4_1^+ \rightarrow 2_1^+)$ value of 160(80) W.u. measured in the same reference. Moreover, Dracoulis *et al.* [Drac 03] have determined the squared prolate amplitude of the yrast 2^+ state to be 0.69 using a formalism reported in Ref. [Drac 94]. The higher spin yrast states are mainly of prolate character. Similar mixing calculations for the 0^+ states in ^{186}Pb have been carried out by Page *et al.* [Page 01] deducing the lowest excited 0^+ state to be approximately 66% of oblate character while the ground state remains essentially as a pure spherical configuration. In addition to the simple mixing calculations based on the experimental data also theoretical studies support the picture of configuration mixing [Hell 05, Bend 04, Rodr 04].

In even-mass Po nuclei, the contribution of the intruder configuration in the ground

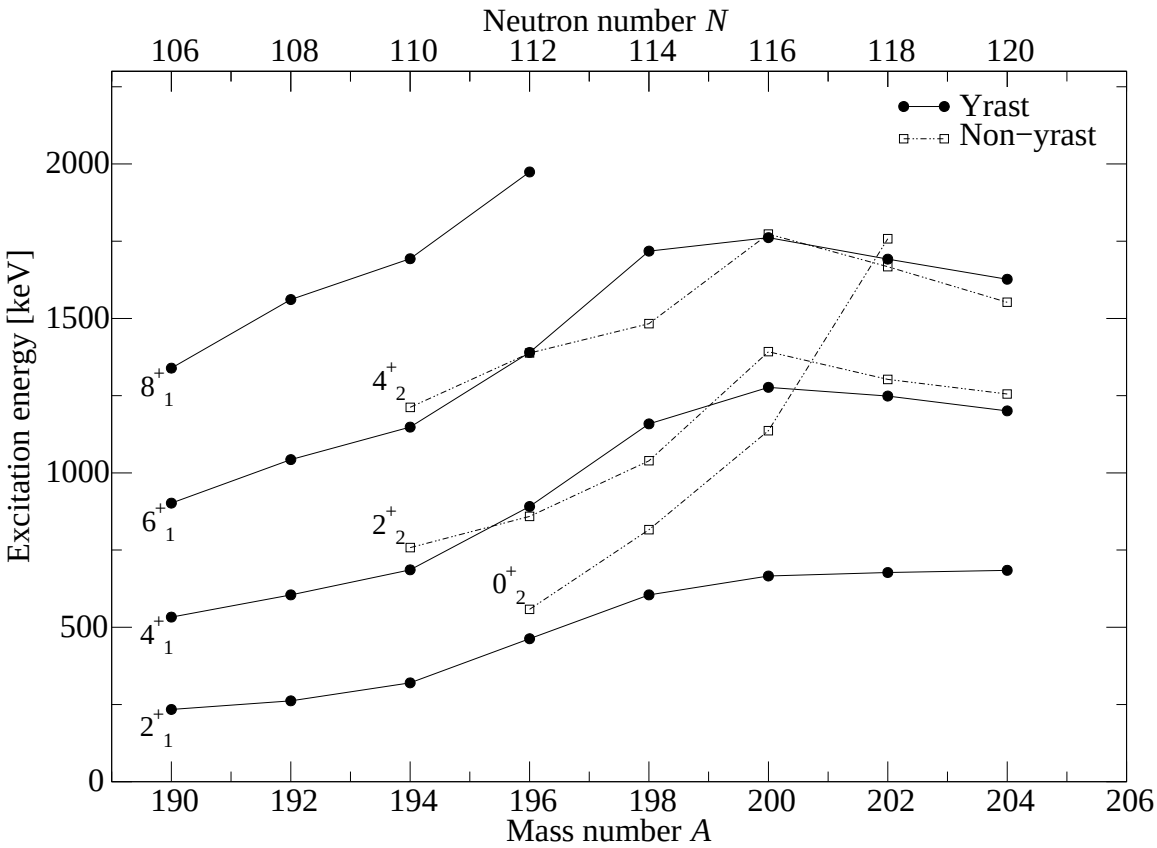

Figure 2.2: A selection of level systematics of the even-mass $^{190-204}$Po isotopes. Data are taken from references [Van 03b, Hela 99, Bern 95, Maj 90, Fant 90, Bijn 98, Bijn 95] and references therein.

state increases when approaching the neutron mid-shell. Bijnens *et al.* [Bijn 95] have determined the intruder contribution to be 29% in ^{194}Po and 58% in ^{192}Po using the energy level systematics. Similarly Allat *et al.* [Alla 98] and Andreyev *et al.* [Andr 99b] determined the intruder configuration in the ground state of ^{192}Po to be $\sim$ 63% and $>$ 65%, respectively, on the basis of α-decay studies. Based on the observed level patterns, Helariutta *et al.* [Hela 99] have deduced an increase of the intruder configuration of the 0_1^+ ground state from 45% in ^{194}Po to 73% in ^{192}Po. The observed 2_1^+ state of ^{194}Po is determined to be 99% of deformed oblate structure. The behaviour of increasing contribution of the deformed structure in yrast states when approaching ^{192}Po is supported by the results obtained with several theoretical models considered by Oros *et al.* [Oros 99].

3 Experimental procedure

The construction of a new efficient spectroscopic facility for tagging studies of heavy nuclei far from stability at the Accelerator laboratory of the University of Jyväskylä gave rise to a successful series of lifetime measurements of excited states in nuclei. This new facility consists of the JUROGAM Ge-detector array coupled to the RITU gas-filled separator [Lein 95] and the GREAT spectrometer [Page 03] at the focal plane of RITU. The Köln plunger device was installed at the JUROGAM target position and coupled to RITU. A triggerless Total Data Readout (TDR) data acquisition system [Laza 01] complements the facility collecting all the data read out from the detectors. Together these equipments constitute one of the most efficient facilities dedicated to tagging experiments near the proton drip-line. In this Chapter the experimental set-up as well as experimental methods are described.

3.1 The JUROGAM germanium detector array

In spring 2003 the JUROGAM germanium detector array was constructed to operate in conjunction with RITU for nuclear structure studies of very neutron-deficient heavy nuclei. In this work all the nuclei under investigation were produced via fusion-evaporation reactions where the beam and target nuclei fuse into a compound nucleus. In this collision, large amount of kinetic energy and angular momentum is transferred to the compound nucleus. Particle evaporation of a few nucleons or α particles occurring after the compound nucleus formation carry away large amount of energy but little angular momentum. The particle evaporation continues until the system reaches the state where the excitation energy is less than the particle separation energy. The remaining excitation energy and angular momentum is then released by a cascade of electromagnetic transitions.

In order to detect prompt γ rays de-exciting the nuclear states the JUROGAM germanium (Ge) detectors are placed in a spherical array around the target. JUROGAM consist of 43 Compton suppressed Ge detectors of EUROGAM Phase I [Beau 92] and GASP type [Alva 93]. Each Ge detector is surrounded by a bismuth germanate (BGO) crystal acting as a veto detector for γ rays scattered from a Ge crystal into the BGO. The supporting structure of the JUROGAM array is a slightly modified EUROGAM Phase I supporting structure. The design of the detector frame is based on an array of regular pentagons with the Ge detectors placed at six different angular positions with

respect to the beam axis (five at 157.6°, ten at 133.6°, ten at 107.9°, five at 94.2°, five at 85.8°and eight at 78.1°). Figure 3.1 shows the JUROGAM array coupled to the RITU separator. A detailed description of the JUROGAM array can be found in Ref. [Paka 05a].

The JUROGAM Ge detectors consist of a large coaxial n-type HPGe crystal of a length $\geq$ 70 mm and a diameter 69 - 75 mm. The efficiency of a JUROGAM Ge-detector ranges from 65% to 85% relative to the efficiency of a 3×3 inch NaI(Tl) detector, measured with a ^{60}Co source (1332 keV γ rays) at a distance of 25 cm. The energy resolution (i.e. Full Width at Half Maximum, FWHM) of a typical JUROGAM detector at 1332 keV varies from 2.5 keV to 3.0 keV. For the needs of the present work the standard JUROGAM target chamber was replaced by a special plunger device described later in this Chapter.

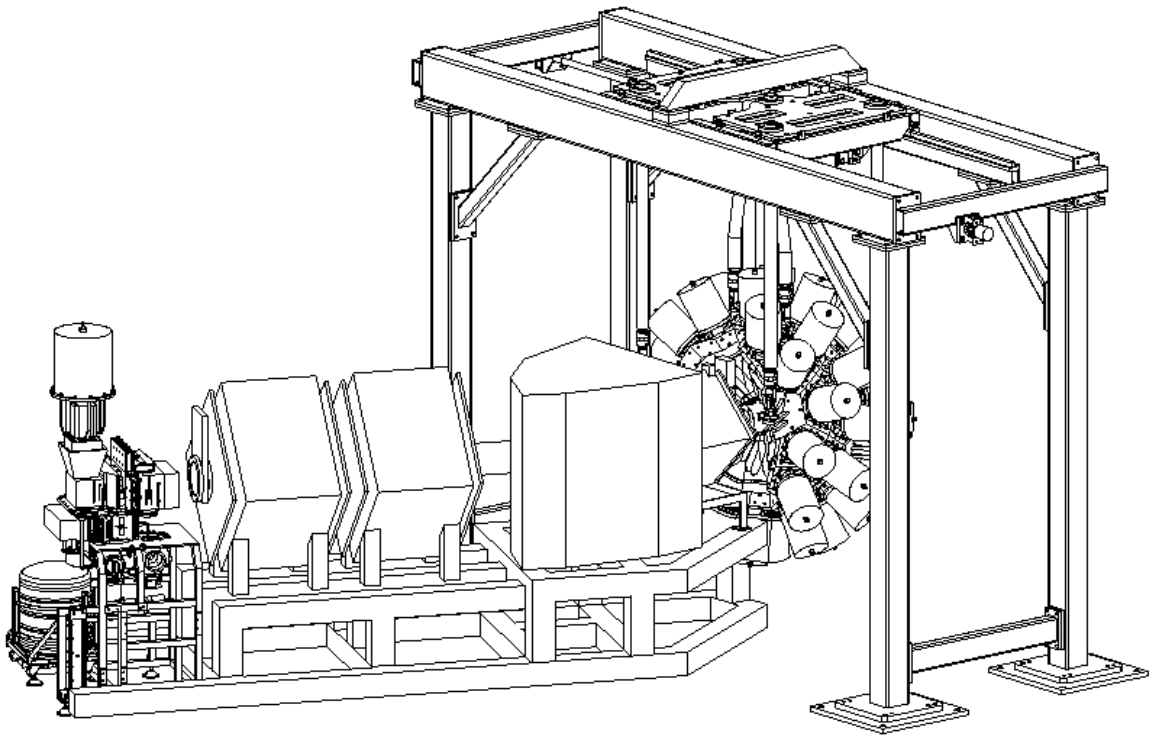

Figure 3.1: The JUROGAM Ge-detector array coupled with the RITU separator.

3.2 The recoil separator RITU

Gas-filled separators are powerful tools in the study of heavy elements produced in fusion-evaporation reactions. The Recoil Ion Transport Unit (RITU) [Lein 95] is a gas-filled recoil separator used in the present work to separate the fusion-evaporation residues from the primary beam and other reaction products, especially fission fragments. The separation and the focusing of the ions is introduced by a magnetic set-up in a QDQQ[1] configuration with a total length of 4.8 m. In the mass region $A \approx 190$ RITU provides a short separation time, typically on the order of 0.5 μs, and a transmission efficiency on the order of 30%. RITU is filled with Helium (He) gas at approximately 0.7 mbar pressure. The high vacuum of the beam line is separated from the gas volume of RITU either a by differential pumping system or a carbon foil. In the present work a 50 μg/cm^2 thick carbon foil was used.

The trajectory of the ion in the magnetic dipole field of RITU is determined by the following relation:

$$B\rho = \frac{mv}{qe}, \tag{3.1}$$

where B is the magnetic flux density, e is the charge of an electron, m and v are the mass and the velocity of the ion, respectively, ρ is the radius of the curvature of the ion path and q is the average charge state. As it can be seen from Eq. 3.1, the broad charge distribution of the ions leads to a wide spatial distribution of the recoils at the focal plane of the separator. However, collisions between reaction products and dilute gas atoms averages the charge state of the reaction products. Therefore several initial charge states will be focused to relatively small area of the focal plane of the separator and the transmission compared to the vacuum mode is enhanced. The average charge state is independent of the initial charge state distribution of the ions at the exit of the target. On the other hand, the charge state focusing leads to the loss of mass resolution. Nevertheless, in tagging studies where the characteristic radioactive decay is used to identify different species the loss of mass resolution is irrelevant.

3.3 The GREAT spectrometer

The Gamma Recoil Electron Alpha Tagging (GREAT) [Page 03] spectrometer comprises a system of silicon, germanium and gas detectors. It is designed to study properties of the reaction products transported to the focal plane of RITU by means of their characteristic radioactive decay. GREAT is optimised to detect the implantation of the reaction product as well as to correlate it spatially and temporarily with any

[1] Q=quadrupole, D=dipole

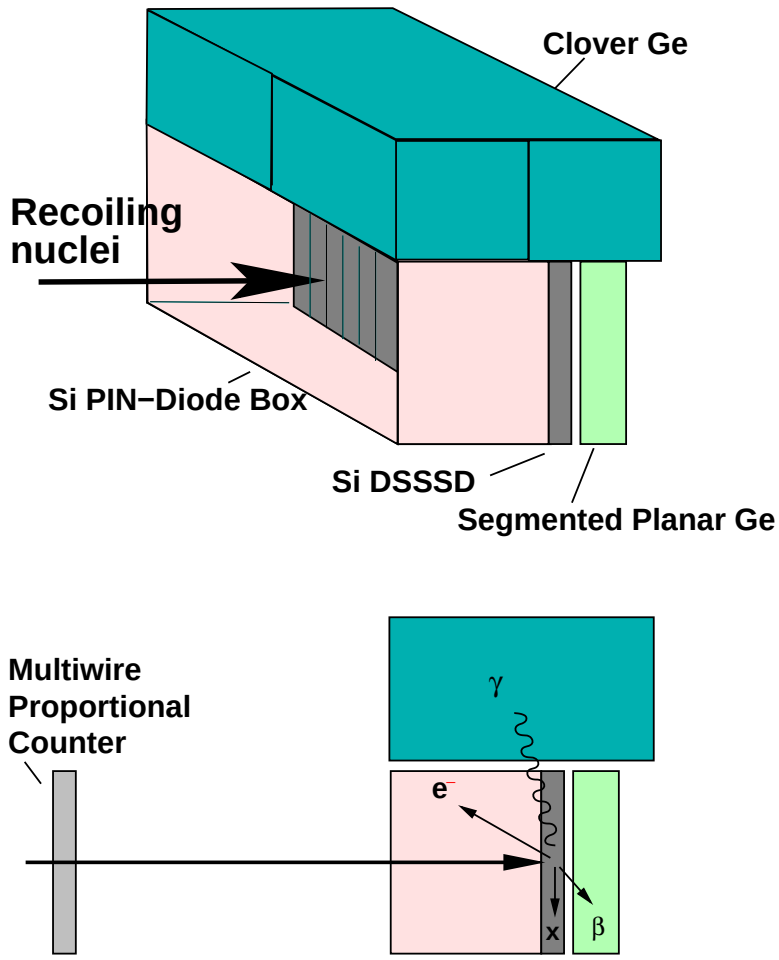

Figure 3.2: The elements of the GREAT spectrometer.

subsequent radioactive decay involving the emission of α and β particles, protons, γ rays, X-rays and conversion electrons. GREAT can either be used in stand-alone focal-plane decay studies, or to provide a selective tag for in-beam spectroscopic studies. GREAT is a powerful tool to study nuclei produced with a very low cross section down to the level of $\sim$ 100 picobarn (for stand-alone decay studies). For in-beam studies corresponding cross-section limit is around 25 nb. The elements of GREAT are discussed below and the schematic drawing is presented in Fig. 3.2.

A **Multiwire Proportional Counter (MWPC)** is positioned at the entrance of GREAT. The MWPC consists of an entrance and an exit Mylar window with an aperture of 131 mm (horizontal) $\times$ 50 mm (vertical) and is filled with isobutane gas. The entrance window separates the MWPC from the He gas of RITU while the exit window protects the high vacuum of other GREAT detectors. When ions pass through the MWPC, energy-loss, timing and position signals are generated.

After passing through the MWPC the recoils are implanted into a pair of **Double-sided Silicon Strip Detectors (DSSDs)** with an active area of 60 mm $\times$ 40 mm and a thickness of 300 μm each. The DSSDs are divided into 60 vertical and 40 horizontal strips with a strip pitch of 1 mm in both directions giving a total of 4800 detector pixels. The DSSDs are used to measure the energies of the implanted recoils and of their subsequent α, β and proton radioactivity. The high granularity of the DSSDs provides a significant improvement in correlation performance compared to previously used focal plane detectors. The two DSSDs, separated by a gap of 4 mm, give a total estimated recoil correlation efficiency of $\approx$ 80%. In addition, a time-of-flight information is generated combining the time information recorded with DSSDs with that of the MWPC. Combining the energy-loss and timing signals of MWPC with the energy measured in the implantation detector a clean separation of recoiling fusion reaction products and scattered beam particles can be made. This, in turn, reduces the background in the spectrum recorded with the implantation detector and, therefore, maximise the efficiency for correlating radioactive decays with the corresponding ion implantation.

Conversion electrons or escaping α particles emitted by a recoil implanted into the DSSDs are detected by an array of 28 silicon **PIN diodes**. The PIN diodes are mounted in a box arrangement around the DSSDs to measure the energies of the conversion electrons and escaped α particles.

Energies of X-rays and low energy γ rays can be measured with a **double-sided planar germanium strip detector**. The planar Ge detector is mounted directly behind the DSSDs. The rectangular crystal has an active area of 120 mm $\times$ 60 mm and a thickness of 15 mm. The crystal of the planar Ge detector is electrically segmented into 12 horizontal and 24 vertical strips.

High energy γ rays can be detected with a **clover Ge detector** mounted above the vacuum chamber housing the DSSDs and PIN diodes. The GREAT clover detector consists of four Ge crystals with a diameter of 70 mm and length of 105 mm. Each of the crystals is electrically four-fold segmented. A BGO Compton suppression shield surrounds the GREAT clover detector.

3.4 Tagging techniques

When studying exotic nuclei close to the proton drip line by in-beam spectroscopic methods employing fusion-evaporation reactions the dominant part of the detected γ rays originate from unwanted fission or Coulomb excitation events. Usually, only a small fraction of the detected γ rays are emitted by the nucleus of interest. In the neutron-deficient Pb region the fission contribution of around 80% of the total

cross-section introduces enormous background in γ-ray spectrum of a typical in-beam measurement. Therefore, several methods to associate the in-beam γ rays with the nucleus of interest have been developed. Within the framework of this study two tagging methods are essential:

Recoil gating

When the nucleus of interest is one of the main fusion-evaporation products, the recoil gating technique provides a selective tag for prompt γ rays detected at the target position. Nuclei recoiling out of the target are filtered with the RITU recoil separator and detected at the focal plane with the GREAT spectrometer. Combining the timing and energy loss signals of the MWPC with the timing signal of the DSSDs a clear separation of fusion products from scattered beam particles can be made. Figure 3.3 illustrates the principle of recoil gating: using the time-of-flight (TOF) and energy loss signals generated by the MWPC and DSSDs a two dimensional spectrum is constructed. Setting the two dimensional gate on the identified recoils, prompt γ rays are associated with the fusion evaporation products. Note that recoil gating technique cannot distinguish between different exit channels of fusion-evaporation reactions because no particle identification at the focal plane of RITU cannot be obtained. Therefore the nucleus of interest has to be the dominant fusion-evaporation product to obtain a clean γ-ray spectrum, i.e. its production cross section should dominate over the other open fusion-evaporation reaction channels. The recoil gating technique has an essential role when the use of the recoil-decay tagging technique is impossible due to the low α-decay branch or long α-decay half-life.

The case of ^{188}Pb studied in the present work is a very good example of the advantage of the recoil gating technique. The α-decay half-life of ^{188}Pb is relatively long (24.2 s) and its α-decay branching amounts to 9.3% only. Under these conditions the use of the recoil-decay tagging technique is not feasible. However, among the fusion evaporation reactions induced by a 340 MeV ^{83}Kr beam on a ^{108}Pd producing ^{188}Pb, i.e. 3n exit channel, has a cross section almost an order of magnitude higher than the other reaction channels. Therefore, recoil gating provides a sufficient reduction of the background events in the γ-ray spectrum of ^{188}Pb.

Recoil-decay tagging

Many nuclei in the neutron-deficient Pb region decay by emitting characteristic α particles. These decay-modes offer an unique signature that a particular nucleus has been produced. The basic idea of the Recoil-Decay Tagging (RDT) method is to identify the recoiling nucleus at the focal plane of a recoil separator by using its

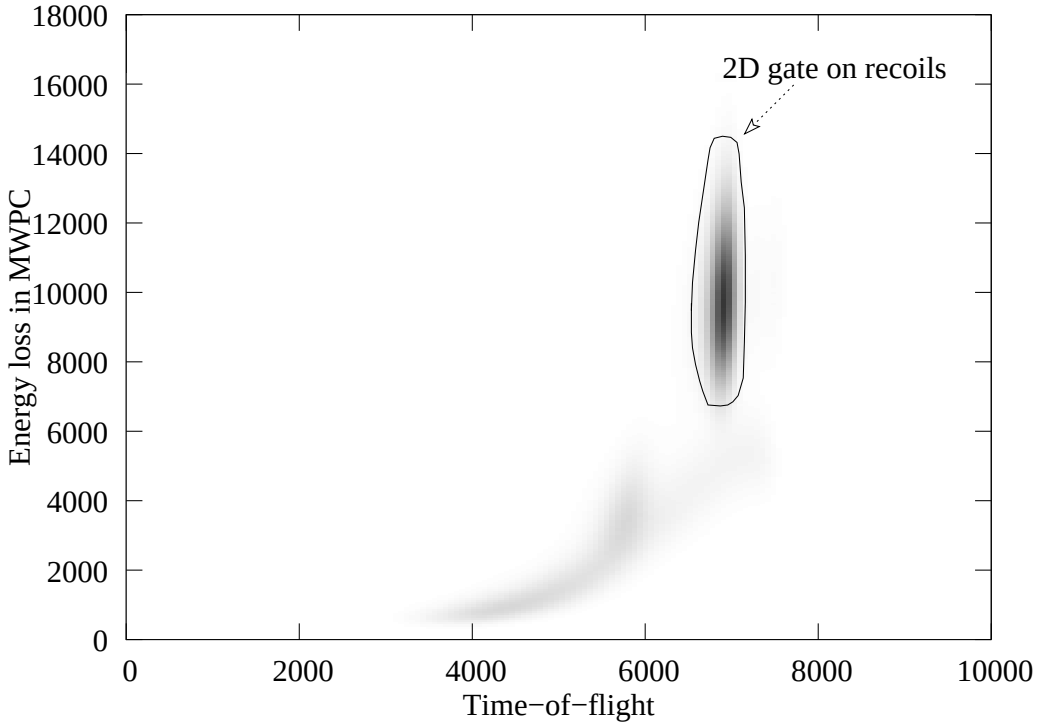

Figure 3.3: A two dimensional plot showing the separation of recoils from the scattered beam as well as the two dimensional gate set on the recoils. The example in this figure is taken from the present study of ^{188}Pb. Events below the recoils originate from the scattered beam and also from the scattered particles from target and degrader materials.

known radioactive decay properties [Simo 86, Paul 95]. Hence, in the present work, the recoils of interest were first selected by means of recoil gating as described in previous Section. The subsequent α decay events originating from the recoils of interest were searched for within the same detector pixel of the DSSDs and within a time interval (search time) of typically 3 - 5 $\times$ $t_{1/2}$ of the α-decay of interest. Finally a tag for prompt γ rays was generated if the α decay (a) passed the energy window, (b) was in anticoincidence with the MWPC signal and (c) occurred within the search time. In this way the prompt γ rays were associated with the nucleus of interest and as a result an essentially background free spectrum was created. Figure 3.4 illustrates the principle of the RDT technique.

The RDT method is suitable for cases where the half-life of the decaying nucleus is short compared to the average time distance between two events detected within the same detector pixel at the focal plane. It is also important to have the α decay branching ratio high enough to maintain a sufficient level of statistics in the tagged γ-ray spectrum. The dominant fission contribution for the reaction products is separated by RITU and thus the counting rate of the DSSDs is reduced to $\sim$ 100 Hz in a typical

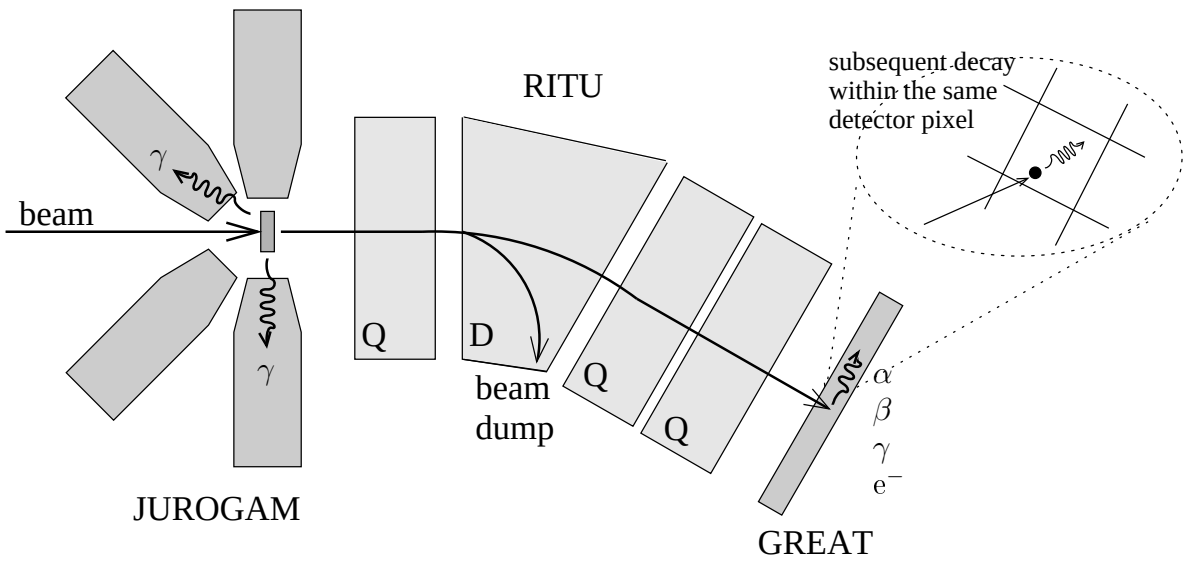

Figure 3.4: The principle of the RDT method: Prompt γ rays are recorded by JUROGAM. Recoiling evaporation residues pass through RITU and are filtered by their m/q ratio before they are implanted into the DSSDs of the GREAT spectrometer. A subsequent radioactive decay within the same detector pixel is detected and the recoil is identified by its characteristic radioactive decay properties. Prompt γ rays are associated with the identified nucleus.

in-beam experiment in the neutron-deficient Pb region. Therefore the high granularity of the GREAT DSSDs (a total of 4800 pixels with a strip pitch of 1 mm in both directions) enables the use of the RDT method for nuclei having a half-life as long as $\sim$ 5 s. These experimental conditions were fulfilled in the case of ^{186}Pb since its α decay half-life is 4.8 s and α decay branching ratio $\approx$ 50%. The typical event rate in the DSSDs was 40 Hz, which implies 25 s for the average time distance between two events within one detector pixel taking into account that events are focused on the central part of the DSSDs (approximately 1000 effective pixels). In the case of ^{194}Po, the experimental conditions concerning the DSSD event rate were even better than in the ^{186}Pb measurement since the corresponding α-decay half-life in only 320 ms and the α branching ratio $\approx$ 100%.

The RDT method has been employed with a great success in various in-beam experiments carried out with JUROGAM as well as various other detector arrays connected to the RITU gas-filled recoil separator [Gree 04]. Recently, also proton and β radioactivity as well as γ-rays emitted from isomeric states have been used in RDT studies to identify the nucleus of interest.

3.5 Data acquisition

In-beam spectroscopic measurements utilising tagging techniques have normally used conventional data acquisition systems with a certain trigger condition and thus have often been limited by the dead time of a data acquisition system. In this work, the triggerless **Total Data Readout (TDR)** data acquisition system [Laza 01] has been employed. The TDR method solves the dead-time problems by reading all the data from every detector independently. The data are time-stamped with a global 100 MHz clock down to a 10 ns accuracy and event fragments are combined together in software.

The front-end electronics of the TDR system (i.e. the constant fraction discriminators (CFDs) and shaping amplifiers) comprises commercial NIM/CAMAC units. The analog-to-digital converter (ADC) cards read all the data timestamping them with the 10 ns accuracy. The metronome unit controls the clock distribution and maintains synchronisation of all the ADCs. The timestamped data received from the ADCs are time ordered in the collate units and sent to the merge unit. The merge unit puts all the data into one time ordered data stream which is then sent to the event builder. Using the spatial and temporal correlations, events are reconstructed in the event builder unit. A simple event could start with a recoil detected at the focal plane. Then by looking back in time, the prompt γ rays within a certain window centred on the time-of-flight of the recoil would be considered to be correlated with the recoil (see the description of the recoil gating method in the previous section). A schematic diagram of the TDR data acquisition system is presented in Fig. 3.5. The data collected in the present work have been sorted under these conditions described in previous Sections.

3.6 The RDDS method

In the **Recoil Distance Doppler-Shift (RDDS) method** [Schw 68], the mean lifetime τ of the nuclear state is related to the time needed by a recoiling nucleus with a velocity $\vec{v}/c$ to travel a certain distance d. In the present work the fusion-evaporation reactions are employed but the following description of the RDDS method holds, in principle, for any nuclear reaction providing sufficient recoil velocity and leaving a nucleus in an excited state.

An evaporation residue formed in a fusion-evaporation reaction recoils out of the production target with a recoil velocity $\vec{v}/c$. In the conventional RDDS technique, the evaporation residues are stopped in a stopper foil located at the distance $d = vt$ from the target. The energy of the γ rays from nuclear levels de-excited before reaching the

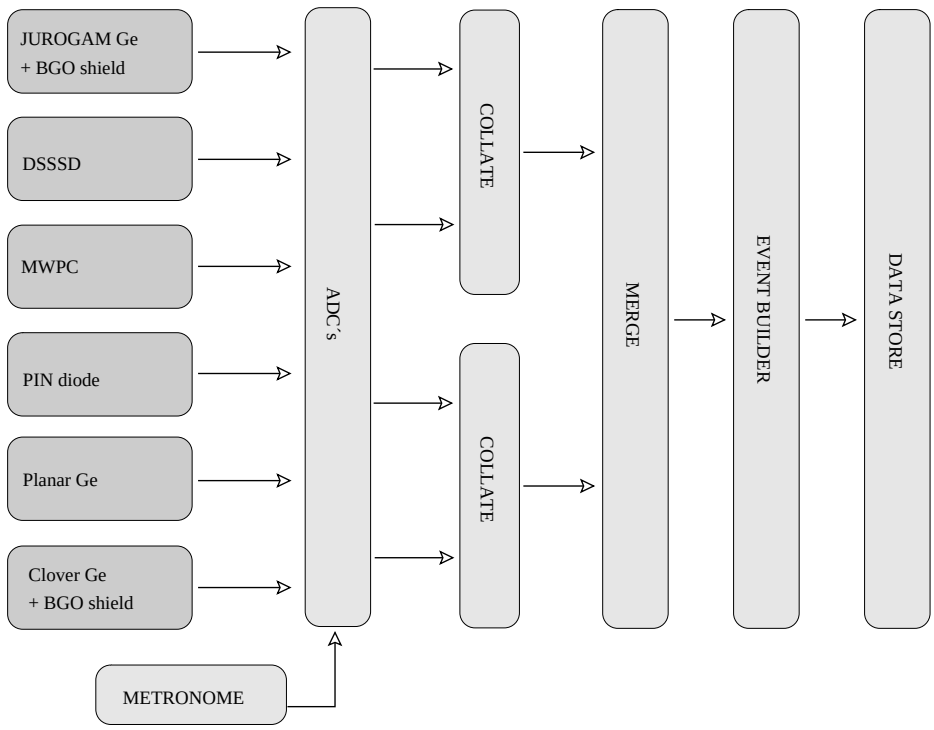

Figure 3.5: A block diagram of the TDR system collecting data from the GREAT and JUROGAM spectrometers. See text for details.

stopper is Doppler-shifted according to the equation

$$E = E_0 \left[1 + \frac{v}{c} \cos\theta\right], \tag{3.2}$$

where E_0 is the energy of the γ-ray emitted from nuclei at rest and θ is the angle of observation of a γ-ray relative to the direction of the velocity $\vec{v}$. In a γ-ray spectrum the fully Doppler-shifted γ rays are separated from those emitted by nuclei stopped in the stopper foil. According to Eq. 3.2 the relative Doppler-shift $\Delta E/E_0$ is directly proportional to the recoil velocity $\vec{v}$. In a fusion-evaporation reaction induced by heavy ion beam such as ^{83}Kr, the recoil velocity is high enough to employ the RDDS method. In the present work it was assumed that a direction of $\vec{v}$ was parallel to the beam (hereafter v).

The intensity of the Doppler-shifted component of the γ-ray of interest follows the relation

$$I_s = I\left[1 - e^{-d/v\tau}\right], \tag{3.3}$$

where I is the total number of emitted γ rays of interest. The intensity of the corresponding unshifted γ rays is

$$I_u = Ie^{-d/v\tau}, \tag{3.4}$$

The mean lifetime τ can be extracted from a measurement of I_s and I_u, or the ratio $I_u/(I_u + I_s)$, as a function of the distance d if the recoil velocity v is known. The distance d can be varied by either moving the target or the stopper in the plunger device dedicated to the RDDS measurements. The recoil velocity can be determined directly from the Doppler-shift observed at a certain angle by using Eq. 3.2.

The first RDDS measurements were applied to the reactions where the nucleus of interest represent a dominant production channel and the recoil velocity is high enough to separate the Doppler-shifted component from the unshifted components of the γ rays of interest. Such measurements have been successful even with low γ-ray detection efficiency. The construction of the large Ge-detector arrays, such as EUROGAM and GAMMASPHERE, have opened up possibilities for RDDS studies in γ-γ coincidence measurements, enabling the extension of the RDDS studies towards more exotic species.

So far, most of the RDDS measurements have been based on the study of prompt γ rays only. However, when studying exotic nuclei such as ^{186,188}Pb and ^{194}Po via fusion-evaporation reactions, the prompt γ-ray spectrum is dominated by a huge background and conventional RDDS measurements are impossible. Therefore it is necessary to somehow "select" the γ rays originating from the nucleus of interest. Such a selection is feasible by employing the tagging methods described in Section 3.4. These methods, in turn, require the use of recoil separators. This makes the use of stopper foils in a plunger device impossible. Hence, in the present work the stopper foil of the conventional plunger device has been replaced by a degrader foil, which allows the evaporation residues to recoil into the recoil separator. As a result the stopped component of a γ-ray transition of interest is replaced by a degraded component and the separation ΔE between the two components is less pronounced than in the conventional case with the stopper foil. To overcome this problem fusion evaporation reactions induced by such a heavy beam as ^{83}Kr are needed to obtain a high recoil velocity. In addition, the material of the degrader can be chosen so that the energy loss of the recoiling nucleus is optimised. Figure 3.6 illustrates the principle of the RDDS method employing a degrader foil.

Perturbing effects

As stated out in Ref. [Jone 69], in principle, several effects have to be taken into account in the analysis of RDDS data. According to the set-up in Fig. 3.6 the solid angle of the detector is larger for the fully Doppler-shifted γ rays than for the degraded ones if detected at the backward angles with respect to the beam direction. This obviously leads to a slight change in the detection efficiency of the fully Doppler-shifted and degraded components of γ-ray transitions. In addition to the static case of positional dependence on the solid angle, one also has to consider the relativistic

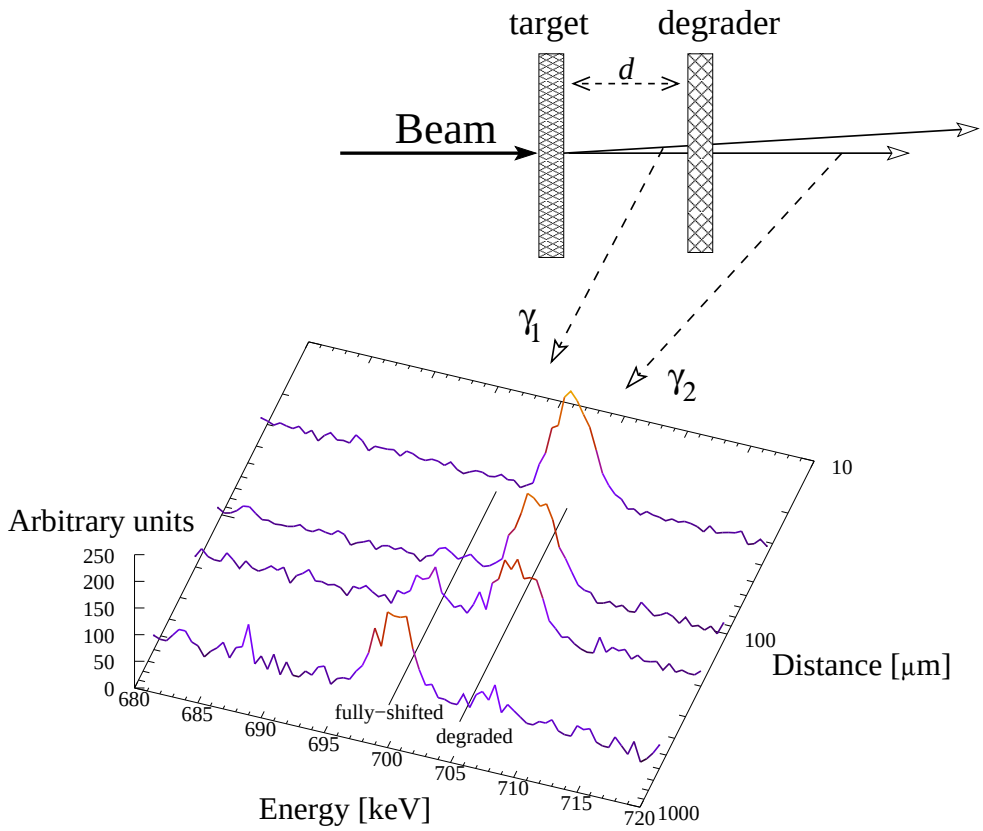

Figure 3.6: The principle of the RDDS method: γ rays originating from a nucleus moving with the initial recoil velocity (γ_1) undergo a different Doppler-shift than γ rays originating from a nucleus moving with degraded velocity (γ_2). By measuring the intensities of both components of the depopulating γ rays as a function of target-to-degrader distance d, the lifetime of a nuclear state can be extracted.

correction of the solid-angle aberration. As a consequence of relativistic transformation of angles between reference frames the effective solid angle is bit different for recoils moving with different velocities. Also the influence of the detection efficiency of the Ge detector for γ rays emitted in flight with different recoil velocities has to be taken into account. After a highly aligning heavy-ion reaction the nuclear spin alignment can be perturbed when the ion recoils into the vacuum. This effect of nuclear deorientation tends to alter the angular distribution and hence the observed γ-ray intensities.

In fact, from all these perturbing effects only the solid-angle effects at long target-to-degrader distances and the nuclear deorientation effect at low spin can have significant influence on the lifetime measured by employing the RDDS method as discussed in Ref. [Petk 92]. However, for the present experiments similarly to the measurement reported in Ref. [Dewa 03], these effects fall within the uncertainties of the derived lifetimes and are therefore neglected in the analysis.

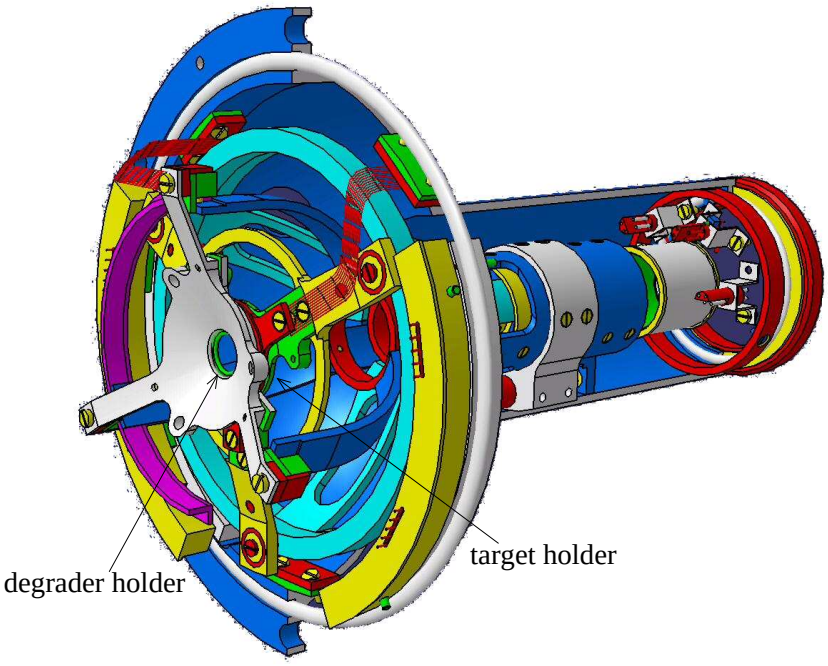

Figure 3.7: Technical drawing of the target and degrader set-up of the Köln plunger device used in the present work [Dewa 06].

3.7 Plunger device

For the present RDDS measurements, the Köln plunger device was installed into the JUROGAM target position. A special chamber housing the target and degrader set-up was designed for this purpose. The target and degrader foils were attached to aluminium rings and then stretched by screwing them on conical support rings (Fig. 3.7). The stretched target and degrader foils were mounted on the frames which, in turn, were attached to two rods. By moving the target by a commercial piezoelectric drive (Inchworm) and keeping the degrader fixed the target-to-degrader distance of interest was selected Short distances $d \lesssim 200$ μm were measured by a magnetic transducer whereas for larger distances an optical system attached to the Inchworm were used.

The plunger device was connected to the gate valve at the entrance of RITU replacing the standard JUROGAM target chamber. Figure 3.8 illustrates the plunger device used in this work and Fig. 3.9 shows the plunger device installed at JUROGAM target position. The target and degrader set-up was positioned in the middle of the JU-

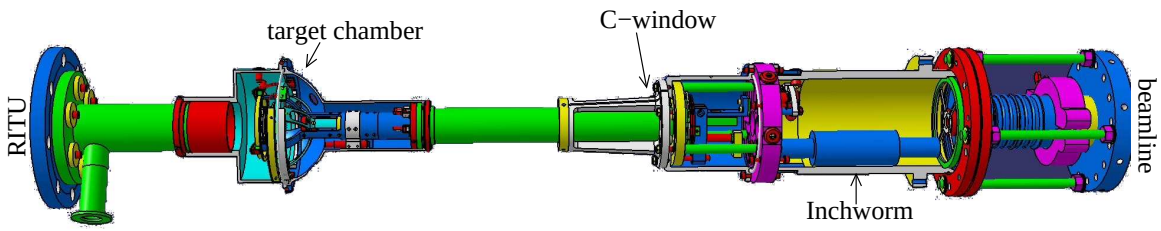

Figure 3.8: Schematic drawing of the plunger device used in this work [Dewa 06]. The left hand side was connected to the gate valve of the entrance of RITU. The right hand side was attached to the beam line. The chamber at the right end of the device housed the electronics and the distance measurement and regulation devices.

ROGAM array. At the other end of the plunger device, a carbon window (50 μg/cm^2) separated the high vacuum of the beam line from the He gas of RITU replacing the differential pumping system nowadays used in RDT measurements at RITU. The vacuum pumping system was designed so that simultaneous pumping down from both sides of the target and degrader setup can be performed. A separate control system of the plunger device recorded the distances of each experimental run. For the shorter distances an automatic regulation of the distance based on the measurement of the capacitance between the target and degrader foils was used.

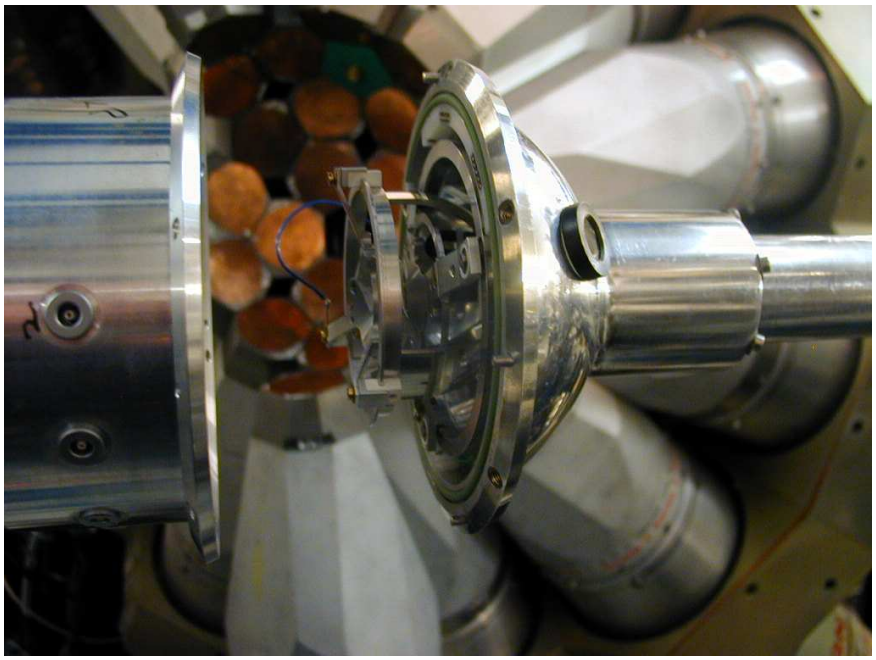

Figure 3.9: The Köln plunger device installed at JUROGAM target position.

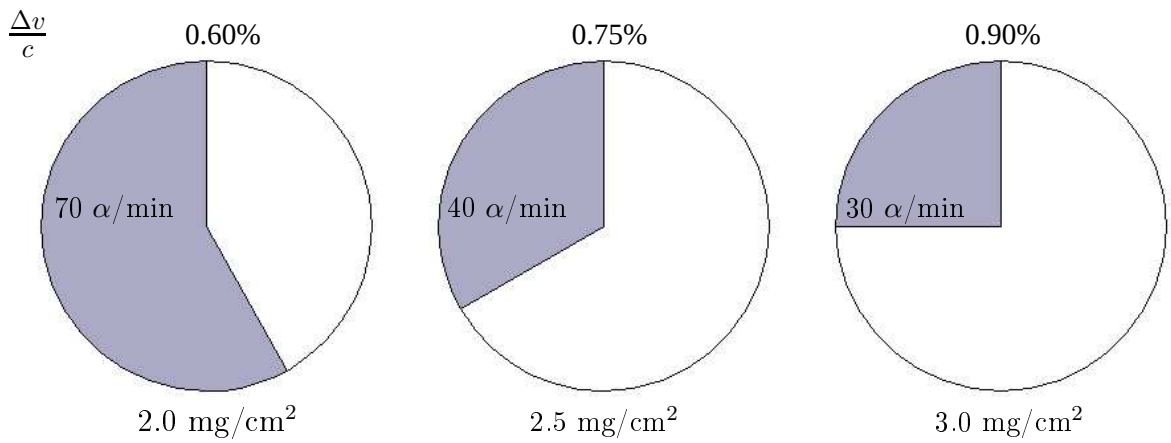

Figure 3.10: Reduction of the α-particle yield at the RITU focal plane with different Au degrader foil thicknesses compared to the yield of 120 α/min with no degrader foil. The numbers at the top of the figure indicate the calculated relative velocity difference of the recoiling nuclei before and after degrader foil.

Reduction of RITU transmission

Transmission for fusion-evaporation residues of RITU was reduced due to the degrader foil used in the plunger device. Due to the small angle scattering in the degrader foil the solid angle covered by the recoiling evaporation residues was increased which, in turn, decreased the number of evaporation residues entering into RITU. Small angle scattering of charged particles in thin foils is described by the equation [Kant 95].

$$\theta_{rms} \propto \frac{zZ}{E}\left(\frac{d}{A}\right), \tag{3.5}$$

where θ_{rms} is the root-mean-square angle of the scattered ion, z and Z are the atomic numbers of the recoiling ion and the medium, respectively, E is the energy of the ion beam, A and d are the mass number and thickness of the foil, respectively.

Prior to the first plunger measurement with JUROGAM a test measurement was carried out in order to optimise both transmission through RITU and the energy separation of the degraded and fully Doppler-shifted components of the γ-ray peaks of interest. A ^{108}Pd target was bombarded by a ^{83}Kr beam with an intensity of ≈ 3 pnA and Au degrader foils of various thicknesses were used. Figure 3.10 summarises the outcome of the test measurement. Based on the test measurement, a 2.5 mg/cm^2 Au degrader foil provided sufficient statistics for the RDDS measurement of ^{188}Pb. A relative calculated velocity difference $\Delta v/c = 0.75\%$ of the recoiling nuclei before and after the 2.5 mg/cm^2 Au degrader foil was obtained.

In the later ^{186}Pb measurement 1.0 mg/cm^2 Al and Mg degraders were tested to in-

crease the transmission of RITU. Since Al and Mg have higher $\mathrm{d}E/\mathrm{d}x$ value than that for Au, thinner degraders could be used and therefore RITU transmission would be increased. As indicated by Eq. 3.5 the lower values for Z and d reduce the θ_{rms} for the evaporation residues. By using a 2.5 mg/cm^2 Au degrader foil with a beam intensity of $I_b \approx 2.5$ pnA ^{186}Pb α particle yield at the RITU focal plane was ≈ 9 α's/min. With 1.0 mg/cm^2 Al and Mg degrader foils and $I_b \approx 2.5$ pnA the corresponding yields were 19 and 24 α's/min. The Al degrader foil is not applicable for short distances since it cannot be stretched. Therefore 1.0 mg/cm^2 Mg degrader was chosen for the following ^{194}Po measurement. In this work, the transmission of RITU is assumed to be around 10% when using the 2.5 mg/cm^2 Au degrader foil while for the 1.0 mg/cm^2 Al and Mg degrader foils the transmission can be estimated to be around 20%.

3.8 The differential decay curve method

In this work, lifetimes of excited states of ^{186,188}Pb and ^{194}Po are derived by using the **Differential Decay Curve Method (DDCM)** [Dewa 89, Petk 92]. In DDCM, the lifetime for each individual level is determined from a single first order differential equation of quantities, which can be obtained from the experimental data, if all direct feeders of the level of interest are known. By DDCM, at each target-to-degrader distance d the mean lifetime τ is determined independently from the equation

$$\tau_i(d) = -\frac{R_{ij}(d) - b_{ij}\sum_h R_{hi}(d)}{v\mathrm{d}R_{ij}(d)/\mathrm{d}t}, \tag{3.6}$$

where $R_{ij}(d)$ is the intensity of the degraded component of the γ-ray transition from a level i to a level j, $R_{hi}(d)$ is the same for the direct feeding transition from a level h to a level i (a schematic level scheme is illustrated in Fig. 3.11) and b_{ij} is the branching ratio of the transition $i \rightarrow j$. The quantities $R_{ij}(d)$ describe the mean time evolution of the number of nuclei in a certain nuclear level and are linked to the decay constants ($\lambda_i = 1/\tau_i$) by a formula

$$R_{ij}(d) = b_{ij}\lambda_i \int_t^\infty n_i(t)\mathrm{d}t, \tag{3.7}$$

where $n_i(t)$ is the number of nuclei at the given state i and $d = vt$. The derivative $\mathrm{d}R_{ij}(d)/\mathrm{d}t$ in the denominator of Eq. 3.6 has to be determined from the measured decay curve by a fitting procedure which fits smoothly connected polynomials through the experimental points without any assumptions. In this way, a smooth differentiable function is created and the values for the derivatives can be obtained.

In the RDDS measurements, spectra are measured at different target-to-degrader distances from which the areas of Doppler shifted $I^s_{ij}(d)$ and degraded $I^d_{ij}(d)$ components of the γ-ray peaks corresponding to the transitions $L_i \rightarrow L_j$ can directly be obtained.

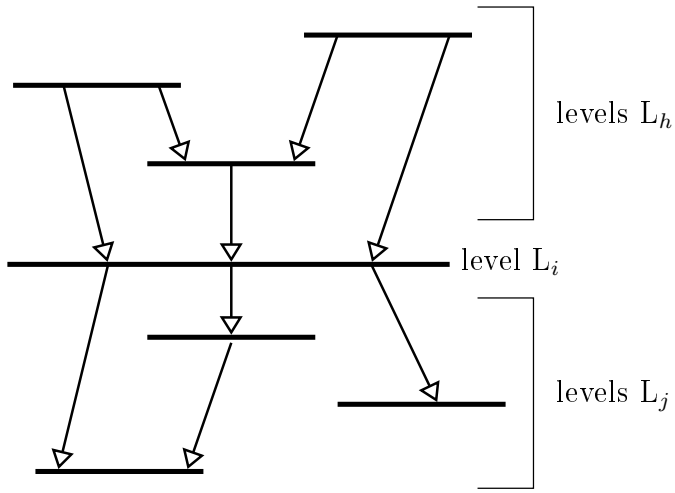

Figure 3.11: A schematic decay scheme

In the analysis of the RDDS data it is conventional to introduce the relative quantities $Q_{ij}(d)$ which are proportional to $R_{ij}(d)$ and can easily be calculated from directly measurable quantities according to the relation

$$Q_{ij}(d) = \frac{R_{ij}(d)}{R_{ij}(0)} = \frac{I^d_{ij}(d)}{I^s_{ij}(d) + I^d_{ij}(d)}. \tag{3.8}$$

Using the quantities $Q_{ij}(d)$, the Eq. 3.6 can be rewritten as

$$\tau_i(d) = -\frac{Q_{ij}(d) - b_{ij} \sum_h [J_{hi}/J_{ij}]\, Q_{hi}(d)}{v \mathrm{d}Q_{ij}(d)/\mathrm{d}t}, \tag{3.9}$$

where J_{hi} and J_{ij} are the relative intensities of the γ-ray transitions $L_h \rightarrow L_i$ and $L_i \rightarrow L_j$, respectively. A detailed presentation of DDCM together with the derivation of the associated equations can be found in Ref. [Dewa 89].

According to Eq. 3.6, the mean lifetime of the level L_i can be obtained at any distance d from the ratio of the quantities $R_{ij}(d) - b_{ij} \sum_i R_{hi}(d)$ and $\mathrm{d}R_{ij}(d)/\mathrm{d}t$. The resulting $\tau(d)$ values should lie on a straight line since, obviously, the lifetime of the level is constant. This is the main advantage of the DDCM since any deviation from the straight line indicates clearly the presence of systematic errors. Moreover, as both the numerator and denominator of Eq. 3.6 reach their maximum at a certain distance one can introduce the concept of a region of sensitivity, i.e. the region where the mean lifetime can be determined with small errors. Such region is illustrated in Fig. 3.12. The principle of lifetime determination according to the DDCM is shown in Fig. 3.13.

Some major advantages of the DDCM analysis are listed below:

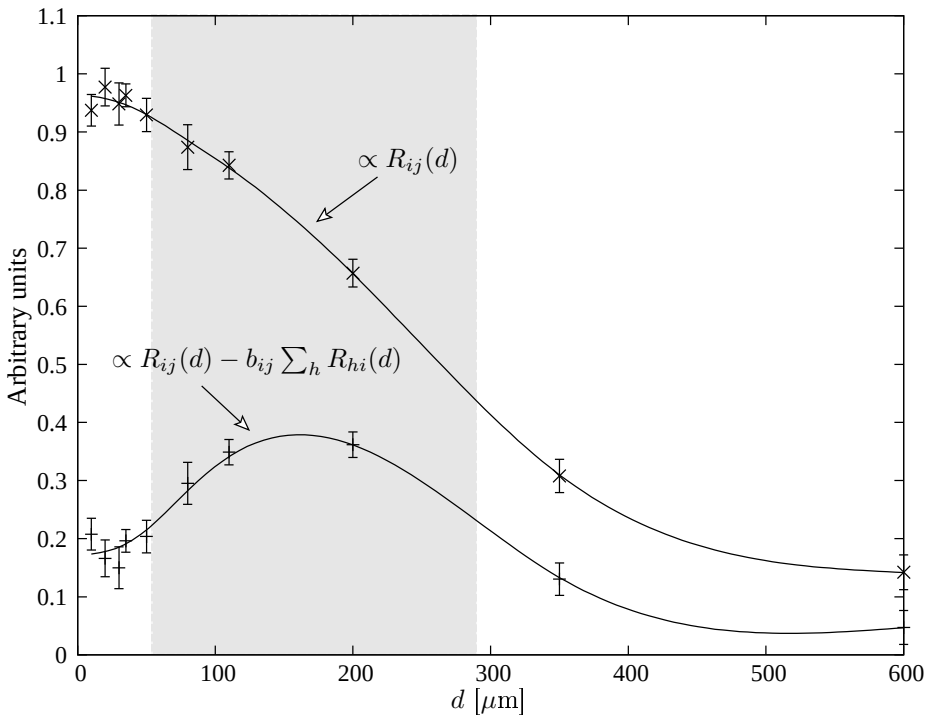

Figure 3.12: A graph of the intensity difference of the feeding and the depopulating transitions as well as the intensity of the depopulating transition of the 4^+ state in ^{188}Pb measured with ten JUROGAM detectors at 134°. These measured intensities are proportional to the quantities in Eq. 3.6. The grey area indicates the region of sensitivity. The smooth lines are only to guide the eye.

- The resulting lifetime τ is not a single value resulting from a fit of an exponential decay curve but a weighted average of the values $\tau(d)$ corresponding to the different target-to-degrader distances d. The values of $\tau(d)$ determined inside the region of sensitivity should be constant. Deviation from such a behaviour is an indication of an error in the analysis. In this way the DDCM enables to identify systematic errors more transparent way as they can be detected as a deviation from the constant values of $\tau(d)$.

- Only direct feeding transitions to the level of interest have to be considered (or in case of missing intensity make assumptions about unobserved feeding). No complex feeding history has to be taken into account.

- Only the relative target-to-degrader distances are important, there is no need to determine any accurate $d = 0$ point.

- The fitting procedure of a decay curve is very transparent. It is important to have a good derivative of a decay curve inside the region of sensitivity, in principle any function(s) can be used. Points outside the region of sensitivity are less important for the fitting procedure.

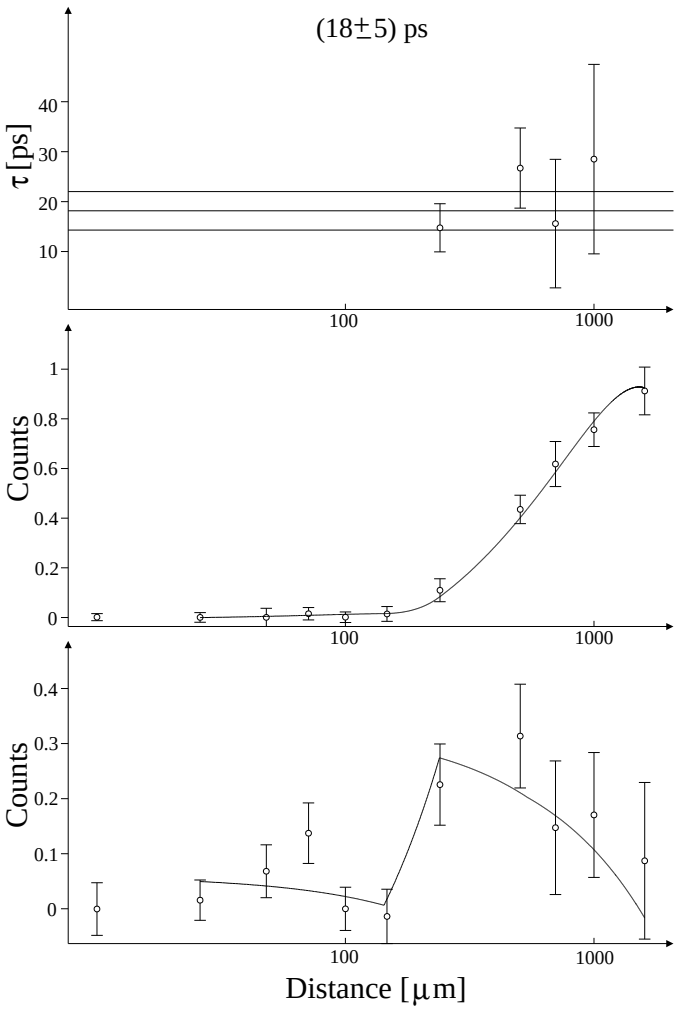

Figure 3.13: Lifetime determination according to the principles of DDCM. The upper panel shows the lifetime τ as a weighted mean of values $\tau(d)$. The central panel shows the decay curve $Q_{ij}(d)$ of the 2^+ state in ^{186}Pb measured with ten JUROGAM detectors at 134°. Intensity difference described by the numerator in Eq. 3.9 is shown in the lower panel. The solid line in the lower panel is the derivative (i.e. denominator in Eq. 3.9) obtained from the fit of the decay curve in the centre panel (solid curve). As it can be seen, the points outside the region of sensitivity are less important.

- Errors of the lifetimes $\tau(d)$ are determined by the statistical errors of the intensities of the degraded and fully Doppler-shifted components of γ rays and the error introduced determining the derivative of the decay curve.
- The lifetime of the considered level can be, in principle, determined with reasonable error only with one target-to-degrader distance inside the region of sensitivity.

DDCM and unobserved feeding

In an RDDS measurement the time behaviour of the depopulating γ-ray transition is characterised e.g. by the drop of the degraded component of the γ-ray peak with increasing target-to-degrader distance. The lifetime of the level experimentally deter-

mined by this way, however, provides information only on the effective lifetime of the initial level. This information includes besides the own lifetime of the level, the complete time behaviour of the feeding transitions. Analysing the exponential behaviour of an RDDS decay curve as presented in Equations 3.3 and 3.4 the lifetimes and the intensities of all the transitions preceding the given level have to be quantitatively considered in order to extract the lifetime of that level from the fit of the decay curve. Therefore, reasonable assumptions about the feeding history have to be made. If the feeding history consists of a complex feeding pattern the number of free parameters becomes large and therefore limits the reliability of the fit. Although in the DDCM only the direct feeding transitions to the level of interest have to be taken into account, in the analysis of singles RDDS data one has to deal with some assumptions concerning unobserved feeding. This is due to the fact that it is impossible to detect all possible feeding transitions to the given level L_i, including the feeding from the continuum or the feeding from unobserved discrete levels, which are too weak to detect.

The intensity of the unobserved feeding (J_i^f) can be obtained from the difference of the relative intensities $\sum_h J_{hi}$ and $\sum_j J_{ij}$ of the populating and depopulating γ-ray transitions, respectively

$$J^f = \sum_j J_{ij}(1+\alpha_{ij}) - \sum_h J_{hi}(1+\alpha_{hi}) = J_{depop} - J_{feed} \tag{3.10}$$

where α_{ij} is the internal conversion coefficient of the transition $L_i \rightarrow L_j$. A problem, which arises from the fact that the lifetime of the unobserved feeding is unknown, can be solved by using several approaches discussed in Ref. [Dewa 89] but the final solution can only be obtained by a coincidence plunger measurement by gating above the level of interest. However, in cases where coincidence data is not available some reasonable assumptions about lifetimes of unobserved feeding transitions can reduce the discrepancy of the results and valuable lifetime information can be obtained.

If only the observed discrete feeding transitions are considered, the unobserved feeding is assumed to be prompt. If the lifetimes of the unobserved feeding transitions are not short compared to the lifetime τ_i and intensity J^f is not small compared to the intensity J_{depop} one has to take them into account in the DDCM analysis and Eq. 3.9 has to be modified. A common hypothesis is that the time dependence of the unobserved feeding is equal to the average lifetime of the direct observed feeders populating the level of interest [Hari 87]. In other words, the decay curve of the missing intensity is obtained as a weighted average of the decay curves of the direct feeding transitions. This assumption is easy to introduce in Equations 3.6 and 3.9 by multiplying the contribution of the feeders in the numerator by the quantity J_{depop}/J_{feed}. This method has been found to be realistic [Petk 92] when there are no special structural effects dominating the feeding pattern of the level of interest. In the present work this assumption is taken for all the considered levels except for the 2^+ state in ^{188}Pb as

will be discussed in the following Chapter. The validity of such an assumption can be checked by inspecting the graph of $\tau(d)$. Deviations from the horizontal line will indicate the presence of components with different lifetimes. Figure 3.13 shows the constant behaviour of $\tau(d)$ which is an indication of the correct assumption made about the unobserved feeding. In this way, DDCM will provide more confidence concerning the assumptions made on the unobserved feeding even in extreme cases where only one feeder is known or the feeding lifetime is particularly long. The detailed discussion about the problem of the unobserved feeding can be found in References [Dewa 89, Petk 92, Hari 87].

3.9 Summary of experimental details

The low production cross sections of ^{186,188}Pb and ^{194}Po require utilisation of tagging techniques to study these nuclei by in-beam spectroscopic methods. In the present experiments carried out at the Accelerator Laboratory of the University of Jyväskylä, the RDT method has been employed in the RDDS lifetime measurements for the first time (^{186}Pb and ^{194}Po) and the recoil gating technique has been used for the RDDS measurement of ^{188}Pb. Excited states of ^{186,188}Pb and ^{194}Po were populated via the fusion-evaporation reactions using the ^{83}Kr beam delivered by the JYFL K130 cyclotron. Experimental details have been presented in Table 3.1. Estimating the cross sections of the employed reactions, 80% detector coverage at the focal plane was assumed. The efficiency to detect α particle with full energy with the DSSDs was assumed to be 55%. For the RITU transmission, the assumptions presented in Section 3.7 were used. Prompt γ rays were detected by the JUROGAM Ge-detector array. The beam intensity varied 1-3 pnA limited mainly by the counting rate of the single JUROGAM Ge detector. Typical energy resolution of JUROGAM detectors used in the present study was 2.7 keV for 1.3 MeV γ rays. Due to their suitable angular position for RDDS measurements, only 15 JUROGAM Ge detectors could be used, five at an angle of 158° and ten at an angle of 134° with respect to the beam direction. The standard JUROGAM target chamber was replaced by the Köln plunger device which housed the target and the degrader set-up. The replacement of a standard stopper foil of the plunger device by a degrader foil allowed fusion-evaporation residues recoil into RITU.

The separated recoils were detected at the RITU focal plane by the GREAT spectrometer. The energy loss and timing signals generated by the recoils in flight were recorded with the MWPC at the entrance of GREAT. After passing through the MWPC the recoils were implanted into the DSSDs which were used to record the position of the recoiling nucleus as well as its subsequent decay properties. Signals from all the detectors were collected and time stamped independently with 10 ns accuracy by employing the TDR data acquisition system. The collected data were analysed of-

fline using the GRAIN [Rahk] software package. Selection of recoils were made using the energy loss and time of flight information provided by the MWPC and DSSDs. Temporal and spatial correlations of a recoil and its subsequent radioactive decay in the DSSDs were performed and singles RDT γ-ray spectra were constructed.

The RDT singles (^{186}Pb and ^{194}Po) and recoil-gated (^{188}Pb) γ-ray spectra from two JUROGAM Ge-detector rings were analysed separately. Several different alternatives for the normalisation factors associated with different target-to-degrader distances were tested (e.g. normalising to the number of γ rays belonging to the Coulomb excitation of the target nuclei or total number of detected α particles). It was found out by inspecting the resulting decay curves that the best distance normalisation is obtained by normalising the intensities of the fully shifted (or degraded) components of the γ-ray transitions under investigation to the sum of the areas of these components These quantities (the functions $Q_{ij}(d)$) are representative for the time behaviour of the corresponding transitions as indicated by Eq. 3.8.

The fitting of the γ-ray peaks was performed carefully by fixing the centroids and widths of degraded and fully-shifted components to obtain the peak areas for both depopulating and feeding transitions of the levels of interest. The fitting parameters were determined from the γ-ray spectra of the experimental runs with shortest and longest target-to-degrader distances for the degraded and fully-shifted components, respectively. In these spectra essentially only one of the components is present.

Decay curves of quantities $Q_{ij}(d)$ were constructed and analysed by means of DDCM. The resulting lifetime of each level is an average of the lifetimes extracted from the decay curves measured with JUROGAM Ge-detectors at 158° and 134°.

Table 3.1: Experimental details of present studies. In order to maximise the transmission of RITU, several types of degrader foils were used in the ^{186}Pb measurement. The values for cross-section σ are rough estimates.

Reaction	E_{beam} [MeV]	σ	v/c	Target thickness [mg/cm^2]	Degrader(s) [mg/cm^2]	Tagging mode
^{106}Pd(^{83}Kr,3n)^{186}Pb	357	120 μb	3.8%	1.0	Au: 2.6, 2.2 mg/cm^2 Al: 1.0 Mg: 1.0	RDT
^{108}Pd(^{83}Kr,3n)^{188}Pb	340	1 mb	3.8%	0.95	Au: 2.5	Recoil gating
^{114}Cd(^{83}Kr,3n)^{194}Po	375	60 μb	3.6%	1.0 + 1.0 Ta support	Mg: 1.0	RDT

4 Results and discussion

In this Chapter a detailed description of the results of the present experiments is given. Each measured energy level is considered separately, paying attention to the treatment of the unobserved feeding transitions. The level of quadrupole collectivity associated with different shapes is considered in terms of transition quadrupole moments. The quadrupole deformation parameter for each level of interest is extracted. Finally, the results of the present experiments are compared to theoretical predictions and to the results of earlier lifetime measurements carried out in the vicinity of neutron-deficient Po and Pb nuclei.

4.1 Lifetimes of the yrast states in ^{188}Pb

In the RDDS measurement of ^{188}Pb recoil gated singles γ-ray spectra were collected at ten target-to-degrader distances ranging from 5 μm to 1600 μm in order to extract lifetimes of excited states in ^{188}Pb. The reaction ^{108}Pd(^{83}Kr,3n)^{188}Pb with a beam energy of 340 MeV was used to populate the yrast states of ^{188}Pb. The statistics obtained with the present experiment were sufficient to extract the lifetimes of four lowest yrast states. A partial level scheme of ^{188}Pb is shown in Fig. 4.1, which illustrates the yrast sequence and a selection of non-yrast states [Drac 04]. Detailed information about experimental runs related to different target-to-degrader distances in the RDDS measurement of ^{188}Pb is given in Table 4.1. A degrader foil of 2.5 mg/cm^2 Au was used in the plunger device to obtain sufficient velocity difference, measured to be $\Delta v/c = 1.0\%$ ($v/c = 3.8\%$ and 2.8% before and after the degrader, respectively). The detailed information of energy differences of the fully Doppler-shifted and degraded components of the γ-ray transitions under investigation is presented in Table 4.2.

Due to the relatively long α-decay half-life ($t_{1/2} = 24$ s) and low α-decay branching ratio (8.5%) of ^{188}Pb the RDT technique is inapplicable. Since the 3n exit channel dominates over other evaporation channels of the employed reaction, sufficient suppression of background γ-ray events was obtained for ^{188}Pb by means of recoil-gating. Samples of such spectra recorded by the five 158° detectors at different target-to-degrader distances are shown in Fig. 4.2. In addition to the reduction of the transmission of RITU, the use of the degrader foil in the plunger device increased the counting rate of the JUROGAM Ge-detectors. It was found out that the 2.5 mg/cm^2 Au degrader foil approximately doubled the counting rate of the JUROGAM Ge-detectors compared

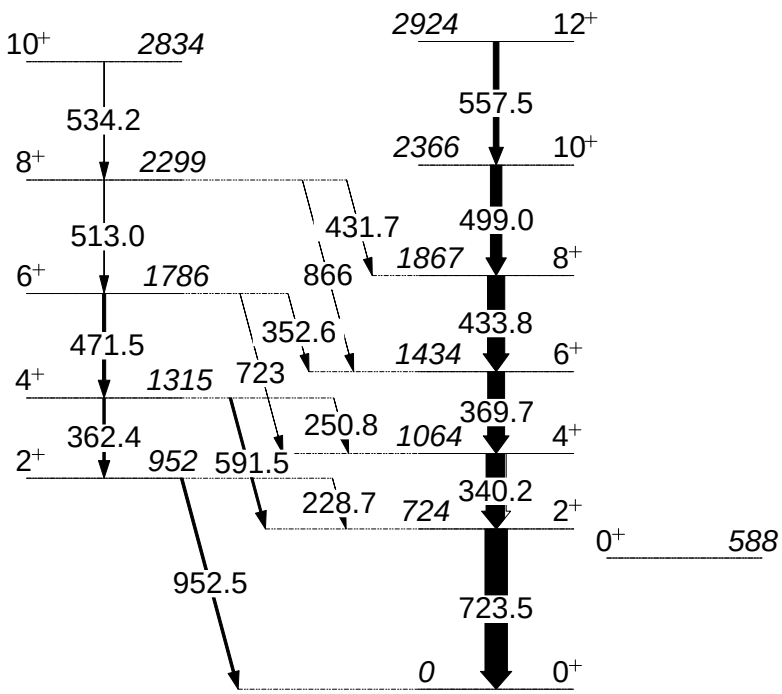

Figure 4.1: Partial level scheme of ^{188}Pb showing the yrast transitions and the dominant feeding transitions to the yrast states according to Ref. [Drac 04]. The excited 0^+ state is taken from Ref. [Van 03a].

Table 4.1: Summary of the measurements of different target-to-degrader distances of the RDDS measurement for ^{188}Pb. The sum of the peak areas of the fully Doppler-shifted and degraded components of the $2^+ \rightarrow 0^+$ transition are measured with ten JUROGAM Ge-detectors at 134°.

Distance d [μm]	Counts $I_u + I_s$, 724 keV $2^+ \rightarrow 0^+$ transition
10.5(2)	1510
20.5(4)	1300
30.5(6)	980
38.0(10)	3240
50.5(10)	1590
80.5(30)	860
113(5)	2150
200(2)	1730
353(8)	970
600(15)	760

Table 4.2: Energy separations ΔE of the fully Doppler-shifted and degraded components and the relative intensities J_γ of γ rays of interest as well as the intensity balance J_{feed}/J_{depop} (see Eq. 3.10) for each level of interest in ^{188}Pb.

E_γ [keV]	J_γ	ΔE at 158° [keV]	ΔE at 134° [keV]	I_i^π	J_{feed}/J_{depop}
724	100	6.5	4.5	2^+	0.82(3)
340	77(2)	3.1	2.3	4^+	0.94(3)
370	74(3)	3.6	2.9	6^+	0.67(3)
434	49(3)	3.9	3.2	8^+	0.53(3)

to the counting rate without the degrader foil. On the other hand, in the plunger measurements it is extremely important to keep the target stretched and stable in order to avoid fluctuations in the target-to-degrader distances. This, in addition to the counting rate limitation introduced by the signal processing electronics of Ge detectors, sets the limit for the beam current used in the present experiments. In the RDDS measurement of ^{188}Pb a 0.95 mg/cm^2 thick stretched self-supporting ^{108}Pd target was used.

Decay curves measured with the JUROGAM Ge-detectors at 158° and 134° were analysed separately by means of DDCM. The distance normalisation was performed by normalising the area of the degraded (or fully Doppler-shifted) component to the sum of the areas of the fully Doppler-shifted and degraded components (see Eq. 3.8). Sample decay curves, i.e. the quantities $Q_{ij}(d)$, are illustrated in Fig. 4.3. Decay curves for both degraded and fully Doppler-shifted components were analysed separately resulting in four lifetime values for each level. The final lifetime is an average of these values.

In order to extract the amount of unobserved feeding to the four lowest yrast states, the relative intensities of the feeding and depopulating transitions were studied. The relative intensities of the transitions were extracted from the experimental run with highest statistics (38.0 μm run). The results are presented in Table 4.2, where J_{feed}/J_{depop} indicates the intensity balance of the levels of interest. For the 4^+, 6^+ and 8^+ states it is realistic to assume the time behaviour of the unobserved feeding to be similar to that for the observed direct feeders as discussed in Section 3.8. For the 2^+ state this assumption is not valid. It was found out that the 2^+ state is populated $\sim 80\%$ from the prolate 4^+ state. The ambiguities arise due to the relative slow feeding from this 4^+ state, which can be seen as a small difference between decay curves of the 2^+ and 4^+ states within the region of sensitivity in Fig. 4.3. Therefore the lifetime of the unobserved feeding transition was varied between 0.1 ps and 16 ps. As a result the extracted lifetime of the 2^+ state varied between 12 ps and 5 ps, respectively. The measured lifetime of 15.9(10) ps for the 4^+ state is in agreement with the value of 16(8) ps obtained in Ref. [Dewa 03], which indicates that the assumption made on the

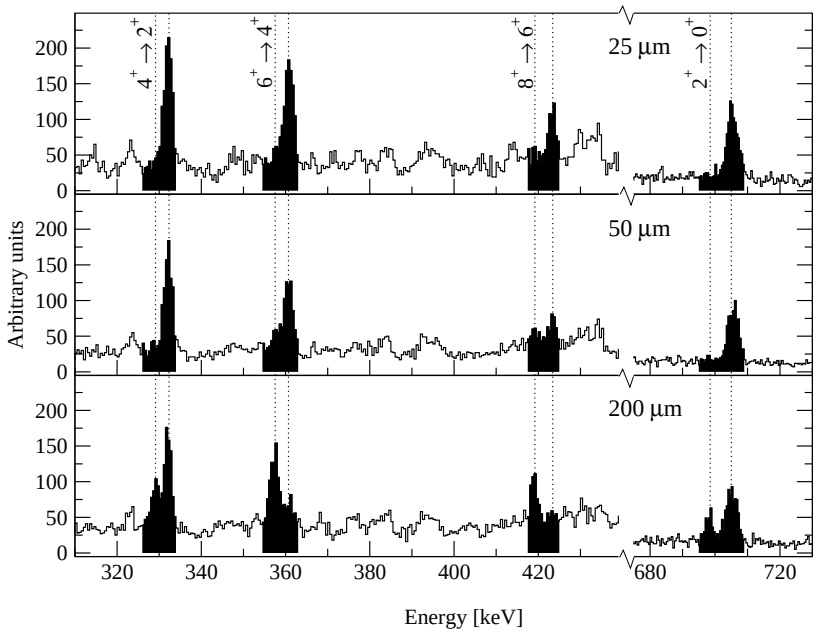

Figure 4.2: Singles recoil-gated γ-ray spectra of ^{188}Pb measured at three distances with five JUROGAM detectors at 158° Dotted lines indicate the positions of the fully Doppler-shifted and degraded components of the γ rays from the yrast 2^+, 4^+, 6^+ and 8^+ states in ^{188}Pb.

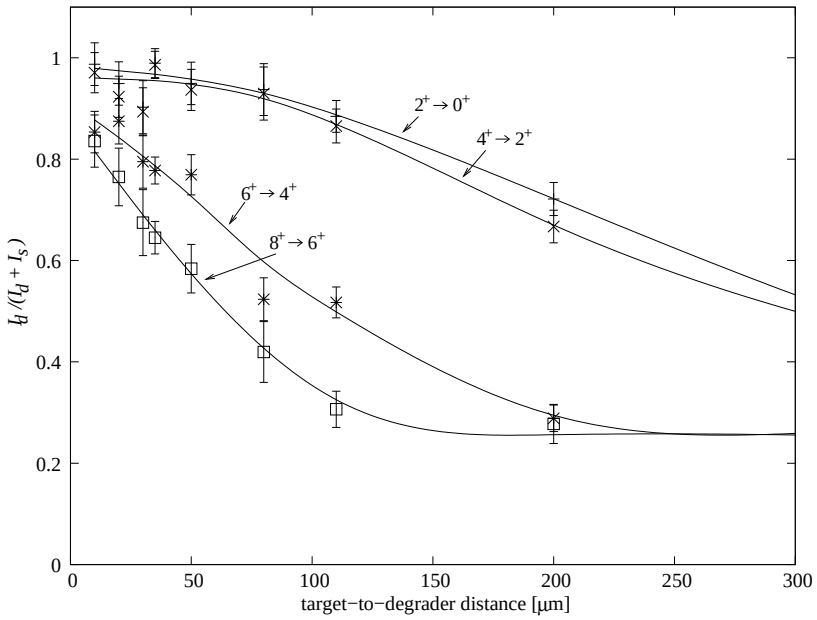

Figure 4.3: Decay curves of four lowest yrast states in ^{188}Pb extracted from γ-ray spectra recorded with five JUROGAM detectors at 158°. The smooth lines are drawn to guide the eye.

side-feeding is reasonable. In the same reference a value of 13(7) ps for the 2^+ state obtained from the coincidence measurement would slightly favour the upper limit of 12 ps determined in the present work.

Table 4.3 summarises the results obtained in the present work for ^{188}Pb. The reduced transition probabilities are extracted using Eq. 2.1 and the transition quadrupole moments using Eq. 2.4. The deformation parameters $|\beta_2|$ are extracted using Eq. 2.7. In this way, the $|\beta_2|$ values presented in Table 4.3 are actually the deformation parameters for the considered transition $I_i \rightarrow I_f$, similar to the $|\beta_t|$ in Ref. [Bend 04].

Table 4.3: Electromagnetic properties of the low-lying yrast states in ^{188}Pb extracted from the present lifetime measurements.

E_γ [keV]	I_i^π	τ [ps]	$B(E2)$ [W.u.]	$\|Q_t\|$ [eb]	$\|\beta_2\|$
724	2^+	5 - 12	12 - 5	2.0 - 1.3	0.07 - 0.04
340	4^+	15.9(10)	160(10)	6.0(2)	0.199(7)
370	6^+	4.0(6)	440(70)	9.4(7)	0.31(3)
434	8^+	2.4(4)	350(60)	8.2(7)	0.27(3)

4.2 Lifetimes of yrast states in ^{186}Pb

The RDT technique was employed for the first time in RDDS measurements to probe lifetimes of low-lying yrast states in ^{186}Pb. Singles RDT γ-ray spectra were collected at 11 target-to-degrader distances. The ^{106}Pd(^{83}Kr,3n)^{186}Pb reaction with a beam energy of 357 MeV was used to populate excited states in ^{186}Pb. A partial level scheme of ^{186}Pb is presented in Fig. 4.4 [Paka 05a]. Table 4.4 summarises the measurements at different target-to-degrader distances. As described in Section 3.7, several degrader foils were tested in order to maximise the transmission of RITU. The target used in the present study was a stretched, self-supporting 1.06 mg/cm^2 ^{106}Pd foil. The limitations concerning the beam current were very similar to those in ^{188}Pb measurement.

Singles RDT γ-ray spectra tagged with the $t_{1/2} = 4.8$ s and $E_\alpha = 6.38$ MeV α-decay of ^{186}Pb were constructed for all 11 target-to-degrader distances. Sample spectra are shown in Fig. 4.5. It is essential to note that in spite of the low number of events in the ^{186}Pb spectra compared to those for ^{188}Pb, the much lower background still enables to resolve the peaks of interest. The production reaction used for this study provided an initial recoil velocity $v/c = 3.8\%$. With all degrader materials, a velocity difference $\Delta v/c \approx 1\%$ was obtained. The energy separations ΔE of the fully Doppler-shifted and degraded components of the γ-rays of interest are listed in Table 4.5. The fitting parameters concerning the lineshape and the centroid of the fully Doppler-shifted and

degraded components of the γ-rays of interest were determined separately for each degrader material and thickness to obtain reliable fits.

As for ^{188}Pb the spectra recorded at 158° and 134° were analysed separately by means of DDCM. The resulting lifetime of each level is an average of these values. The areas of the degraded components were normalised to the sum of the fully Doppler-shifted

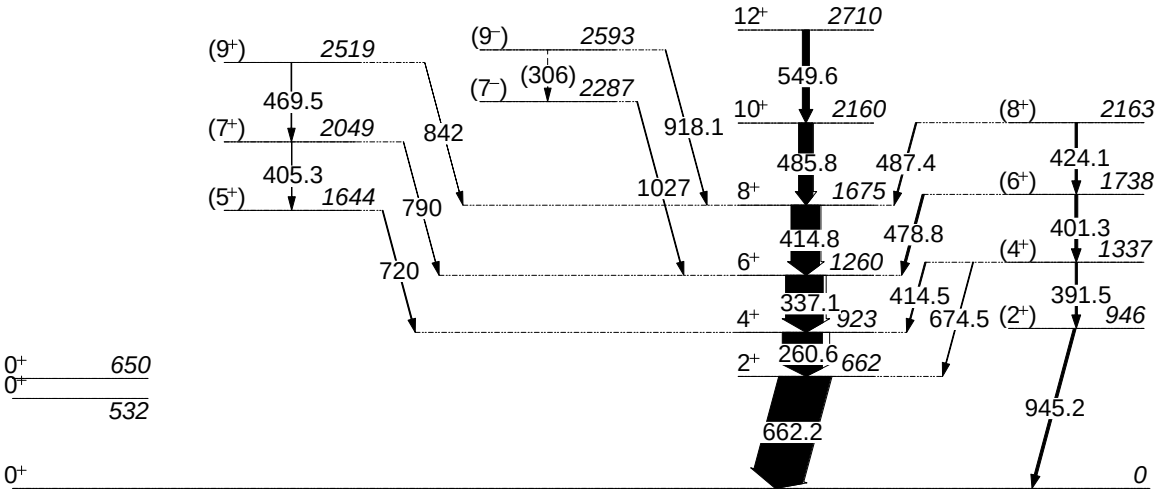

Figure 4.4: Partial level scheme of ^{186}Pb [Paka 05a] showing the yrast states and major feeding transitions to the yrast states. Excited 0^+ states are taken from Ref. [Andr 00].

Table 4.4: Summary of the measurements of different target-to-degrader distances of the RDDS measurement for ^{186}Pb. The sum of the peak areas of the fully Doppler-shifted and degraded components of the $2^+ \rightarrow 0^+$ transition are measured with ten JUROGAM Ge-detectors at 134°.

Distance d [μm]	Counts $I_u + I_s$, 662 keV $2^+ \rightarrow 0^+$ transition	Degrader
10.0(5)	70	2.6 mg/cm^2 Au
26.0(15)	256	1.0 mg/cm^2 Mg
48(3)	209	2.2 mg/cm^2 Au
71(3)	204	1.0 mg/cm^2 Mg
100(2)	75	2.6 mg/cm^2 Au
147(3)	182	1.0 mg/cm^2 Mg
240(5)	126	2.6 mg/cm^2 Au
505(40)	175	1.0 mg/cm^2 Al
700(40)	144	1.0 mg/cm^2 Al
1000(40)	179	1.0 mg/cm^2 Al
1600(40)	115	1.0 mg/cm^2 Mg

Table 4.5: Energy separations ΔE of the fully Doppler-shifted and degraded components and the relative intensities J_γ of γ rays of interest as well as the intensity balance J_{feed}/J_{depop} (see Eq. 3.10) of each energy level of interest in ^{186}Pb.

E_γ [keV]	J_γ	ΔE at 158° [keV]	ΔE at 134° [keV]	I_i^π	J_{feed}/J_{depop}
662	100	5.6	4.0	2^+	0.95(9)
261	82(6)	2.1	2.0	4^+	0.78(9)
337	69(6)	2.6	2.5	6^+	0.80(10)
415	57(5)	3.0	2.7	8^+	0.57(5)

Table 4.6: Electromagnetic properties of the low-lying yrast states in ^{186}Pb extracted from the present lifetime measurements.

E_γ [keV]	I_i^π	τ [ps]	$B(E2)$ [W.u.]	$\lvert Q_t \rvert$ [eb]	$\lvert\beta_2\rvert$
662	2^+	18(5)	6(2)	1.3(2)	0.045(7)
261	4^+	18(4)	510(120)	10.3(2)	0.34(4)
337	6^+	6(2)	460(160)	10(2)	0.31(5)
415	8^+	5(2)	200(140)	6(2)	0.21(5)

and degraded components of the γ-ray transition of interest and the decay curves of $Q_{ij}(d)$ were constructed. Sample decay curves are presented in Fig. 4.6.

Again, relative intensities of the γ-ray transitions were studied in order to determine the amount of unobserved feeding to the states of interest. Table 4.5 lists the values for the relative intensities of γ-rays and the quantities J_{feed}/J_{depop}, which are determined from the data of the experimental run with highest statistics (26.0 μm run). For all the states in ^{186}Pb probed in the present study, a similar time behaviour for the unobserved feeding transitions was assumed than that for the observed ones. It was found out that the effect of varying the lifetime of unobserved feeding transitions between the prompt feeding and similar to the observed feeding is negligible in the sense that the resulting lifetimes fall within the statistical error bars of the derived lifetimes.

In Table 4.6 the results for the lifetimes τ, absolute transition probabilities $B(E2)$ and deformation parameters $|\beta_2|$ for ^{186}Pb extracted in a similar manner as for ^{188}Pb are presented.

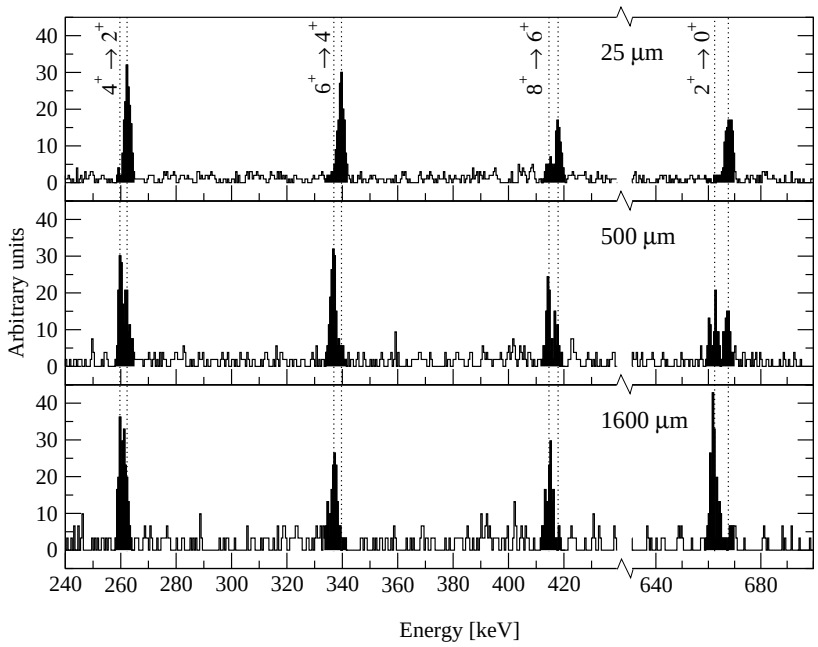

Figure 4.5: Singles RDT γ-ray spectra of ^{186}Pb measured at three distances with five JUROGAM detectors at 158° Dotted lines indicate the positions of the fully Doppler-shifted and degraded components of the γ rays from the yrast 2^+, 4^+, 6^+ and 8^+ states in ^{186}Pb.

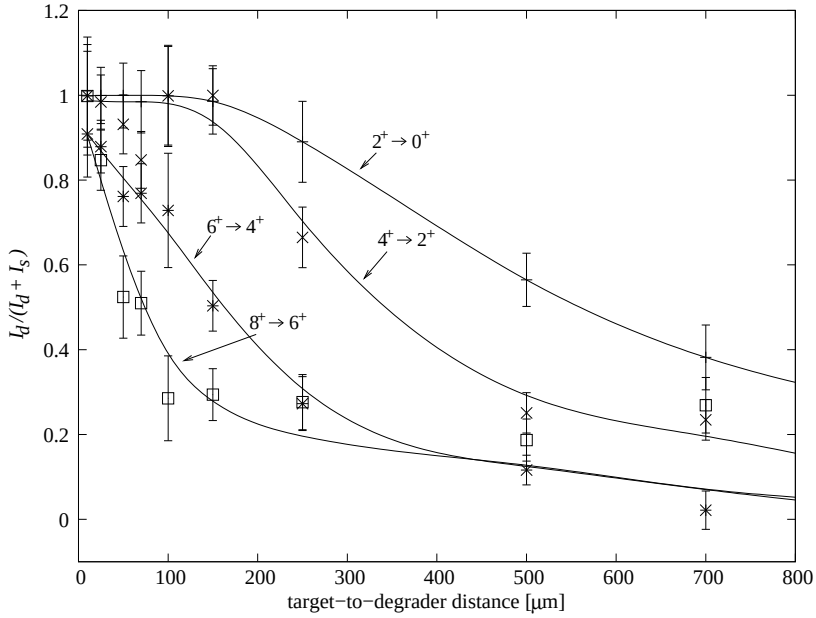

Figure 4.6: Decay curves of four lowest yrast states in ^{186}Pb extracted from γ-ray spectra recorded with ten JUROGAM detectors at 134°. The smooth lines drawn to guide the eye.

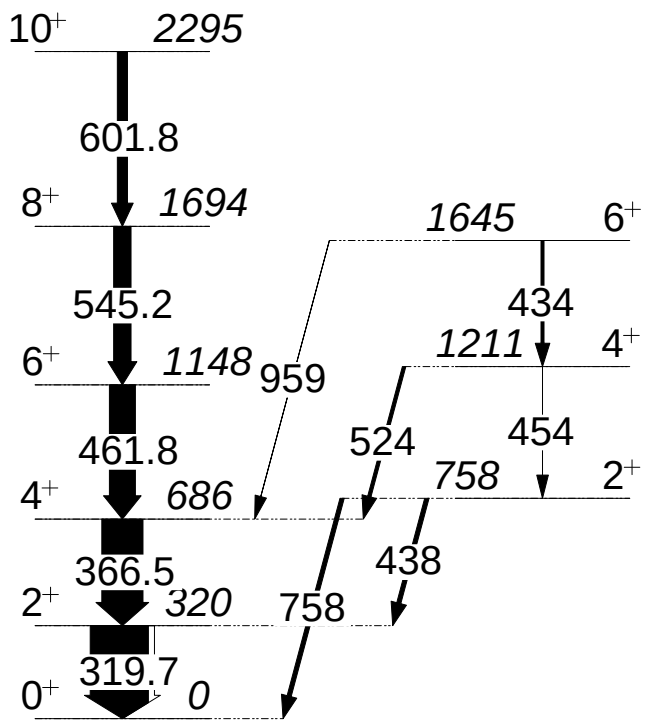

Figure 4.7: Partial level scheme of ^{194}Po [Hela 99] showing the yrast states and major feeding transition to the yrast states.

4.3 Lifetimes of low-lying states in ^{194}Po

The ^{194}Po α-decay with $t_{1/2}$= 390 ms and E_α = 6.99 MeV was used to tag the prompt γ rays of interest to obtain singles RDT γ-ray spectra for 13 target-to-degrader distances. The fusion-evaporation reaction ^{114}Cd(^{83}Kr,3n)^{194}Po with a ^{83}Kr beam energy of 375 MeV was used to populate excited states in ^{194}Po. A partial level scheme of ^{194}Po is presented in Fig. 4.7 [Hela 99] and a summary the experiment is given in Table 4.7.

To obtain the sufficient recoil velocity a heavy ion beam such as ^{83}Kr has to be used. This, in turn, sets the limits to the choice of the target nuclei. With the ^{83}Kr beam the target nucleus has to be ^{114}Cd in order to produce ^{194}Po via the 3n evaporation channel. However, a metallic Cd foil cannot be stretched and therefore cannot be used as a target in a plunger device. In the present work a 1.0 mg/cm^2 stretched Ta foil facing the beam was used to support a 1.0 mg/cm^2 ^{114}Cd target. It was found out that the use of Ta support at least doubled the counting rate of the Ge detectors compared to the situation when there is no Ta support. This, in addition to the increase of the Ge detector counting rate introduced by the degrader foil as discussed earlier, limited the beam current to 2 pnA in the present RDDS measurement of ^{194}Po.

Table 4.7: Summary of the measurements of different target-to-degrader distances of the RDDS measurement for ^{194}Po. The sum of the peak areas of the fully Doppler-shifted and degraded components of the $2^+ \rightarrow 0^+$ transition are measured with ten JUROGAM Ge-detectors at 134°.

Distance d [μm]	Counts $I_u + I_s$, 320 keV $2^+ \rightarrow 0^+$ transition
5.7(5)	263
7.4(15)	122
28(1)	365
43.2(12)	442
52.7(13)	215
133(2)	333
173(2)	207
253(3)	391
400(5)	186
700(10)	195
1000(10)	358
1490(15)	114
3000(40)	103

Table 4.8: Energy separations ΔE of the fully Doppler-shifted and degraded components and the relative intensities J_γ of γ rays of interest as well as the intensity balance J_{feed}/J_{depop} (see Eq. 3.10) of each energy level of interest in ^{186}Pb.

E_γ [keV]	J_γ	ΔE at 158° [keV]	ΔE at 134° [keV]	I_i^π	J_{feed}/J_{depop}
320	100	2.8	2.1	2^+	0.78(6)
367	80(5)	3.3	2.7	4^+	0.60(6)

The production reaction employed in the present study of ^{194}Po provided an initial recoil velocity of $v/c = 3.6$ %. Based on the experience gained in the RDDS measurement of ^{186}Pb, a 1 mg/cm^2 Mg degrader foil was used to obtain the velocity difference of $\Delta v/c = 0.8$ %. The separations ΔE of the fully Doppler-shifted and degraded components of the γ-rays of interest are given in Table 4.8.

In the present study the production cross-section of ^{194}Po was approximately 60 μb representing an all time record in an RDDS measurement. Despite of very low statistics, the low background in RDT γ ray-spectra still enabled to resolve the fully Doppler-shifted and degraded components of γ-rays from the lowest 2^+ and 4^+ states in ^{194}Po. Sample γ-ray spectra are shown in Fig. 4.8.

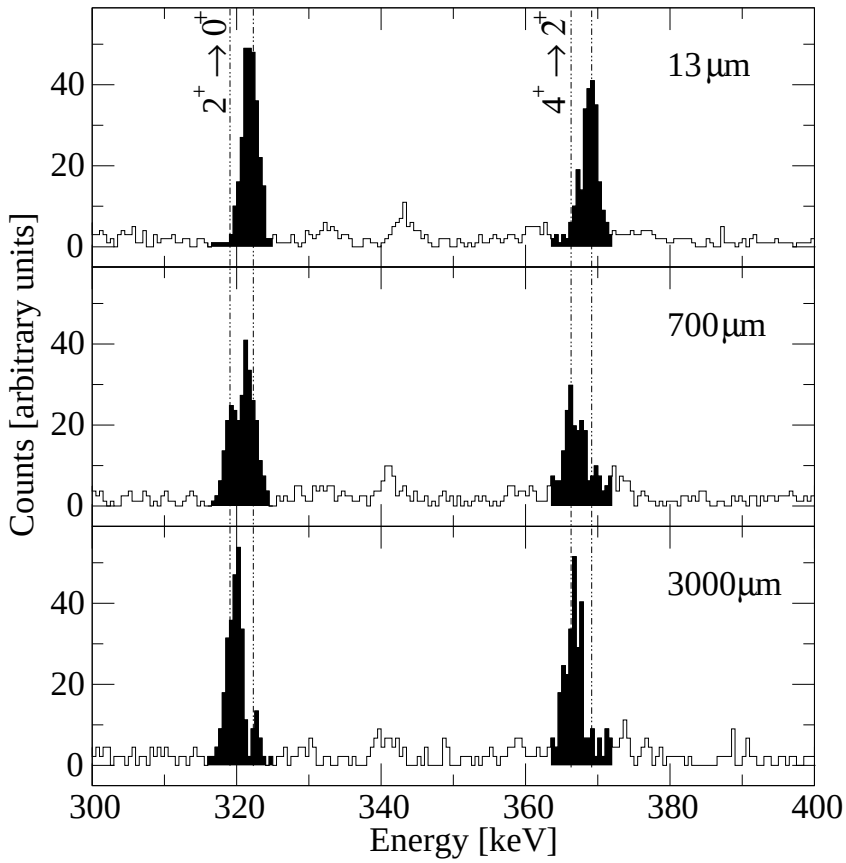

Figure 4.8: Singles RDT γ-ray spectra of ^{194}Po measured at three distances with five JUROGAM detectors at 158° Dotted lines indicate the positions of the fully Doppler-shifted and degraded components of γ rays from the first excited 2^+ and 4^+ states in ^{194}Po.

As in the earlier measurements, spectra recorded with the JUROGAM detectors at 158° and 134° were analysed separately by means of DDCM. The distance normalisation was performed similarly to the ^{188}Pb and ^{186}Pb measurements and decay curves of $Q_{ij}(d)$ were constructed. The resulting lifetime is an average of the values extracted from the spectra recorded at 158° and 134°. An example of the decay curves is presented in Fig. 4.9.

In Table 4.8 the values of relative intensities of the γ-ray transitions under investigation as well as the intensity balances J_{feed}/J_{depop} for the states of interest are shown. These values were extracted from the experimental run with highest statistics (43.2 μm run). The treatment of unobserved feeding transitions is similar to that for ^{186}Pb, i.e. the time behaviour of unobserved feeding is assumed to be similar to the observed one. In addition, it was found out that the effect of varying the time behaviour of the unobserved feeding transitions is negligible within the error bars of the derived lifetimes.

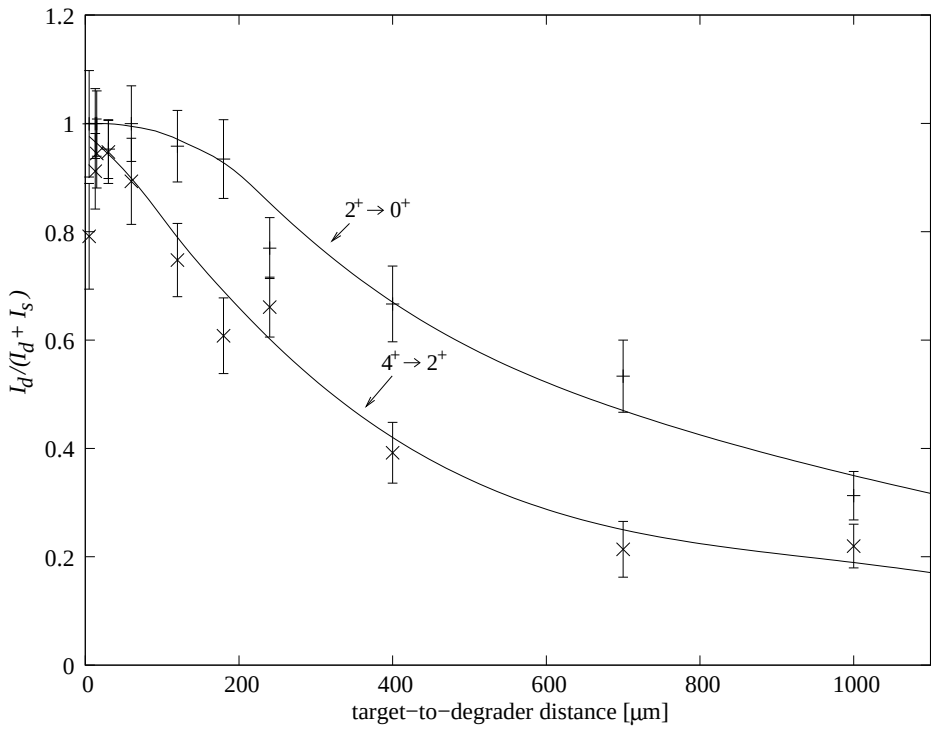

Figure 4.9: Decay curves of two lowest yrast states in ^{194}Po extracted from spectra recorded with ten JUROGAM detectors at 134°. The smooth lines are drawn to guide the eye.

Table 4.9 lists the values of τ, $B(E2)$, Q_t and β_2 extracted for the two lowest yrast states in ^{194}Po.

Table 4.9: Electromagnetic properties of the low-lying yrast states in ^{194}Po extracted from the present lifetime measurements.

E_γ [keV]	I_i^π	τ [ps]	$B(E2)$ [W.u.]	$\lvert Q_t \rvert$ [eb]	$\lvert \beta_2 \rvert$
662	2^+	37(7)	90(20)	5.5(6)	0.17(2)
261	4^+	14(4)	120(40)	5.4(8)	0.17(3)

4.4 Discussion and conclusions

4.4.1 Configuration mixing and collectivity in light Pb nuclei

In the framework of coexisting spherical, oblate and prolate shapes, interesting conclusions from the present results can be drawn. The large $E2$ transition strengths of the $8^+ \rightarrow 6^+$ and $6^+ \rightarrow 4^+$ transitions in ^{186,188}Pb reveal high collectivity of the yrast 4^+, 6^+ and 8^+ states in these nuclei and are in agreement with the hypothesis of prolate yrast states. A similar high $E2$-strength is observed for the $4^+ \rightarrow 2^+$ transition in ^{186}Pb indicating that the 2^+ state in ^{186}Pb is a pure member of the prolate band. However, in ^{188}Pb the $4^+ \rightarrow 2^+$ transition rate is significantly lower than that in ^{186}Pb suggesting a strongly mixed character for the first excited 2^+ state in ^{188}Pb. The predicted spherical ground state in Pb nuclei is reflected by the low $2^+ \rightarrow 0^+$ transition rate in ^{186,188}Pb.

It is supported by many theoretical studies (see e.g. [Hell 05, Bend 04]) that the contribution of the spherical component in the wave function of the observed excited states is insignificant. Therefore, it is eligible to interpret the observed $B(E2)$ values in ^{188}Pb in a simple two level (prolate $\pi(4p-4h)$ and oblate $\pi(2p-2h)$) mixing scheme introduced in Section 2.3. By treating the 6^+ and 8^+ states as pure prolate states an average Q_t^{def} value for prolate states can be derived as $Q_t^{def} \approx 8.8$ eb. By using Eq. 2.14 a squared prolate amplitude $\alpha^2_{prolate} \approx 0.4$ can be derived for the 2^+ yrast state in ^{188}Pb. This is somewhat smaller than that determined in References [Dewa 03, Drac 04] where different assumptions were made to extract the mixing amplitude. The $\alpha^2_{prolate}$ value of 0.4 determined in this work takes into account the level of collectivity obtained for the $6^+ \rightarrow 4^+$ and $8^+ \rightarrow 6^+$ transitions which is remarkably higher than that for the $4^+ \rightarrow 2^+$ transition.

Experimentally the degree of deformation in neutron-deficient Pb and Po nuclei has been deduced from the kinematic moments of inertia $\mathcal{J}^{(1)}$, which in general, is larger for prolate than oblate bands. Figure 4.10 shows $\mathcal{J}^{(1)}$ values for typical prolate and oblate bands in neutron mid-shell nuclei near $Z = 82$ extracted from the measurements using Eq. 2.12. As stated in Section 2.2, the contribution of the deformation parameter β_2 to $\mathcal{J}^{(1)}$ is small. From Fig. 4.10 it can be seen that the difference between $\mathcal{J}^{(1)}$ for prolate and oblate shapes is, however, well pronounced. This clearly indicates the fact that other effects, as described in Section 2.2, contribute to $\mathcal{J}^{(1)}$ rather strongly.

If a nuclear system has an intrinsic structure in the band that is not changing and the system receives collectivity via pure rotation, the quadrupole moment within the band should be constant. The measured $|Q_t|$ values for ^{186,188}Pb are plotted in Fig. 4.11 in conjunction with the kinematic moments of inertia $\mathcal{J}^{(1)}$ deduced from the measured level energies [Paka 05b, Drac 04]. The strongly mixed character of the 2^+

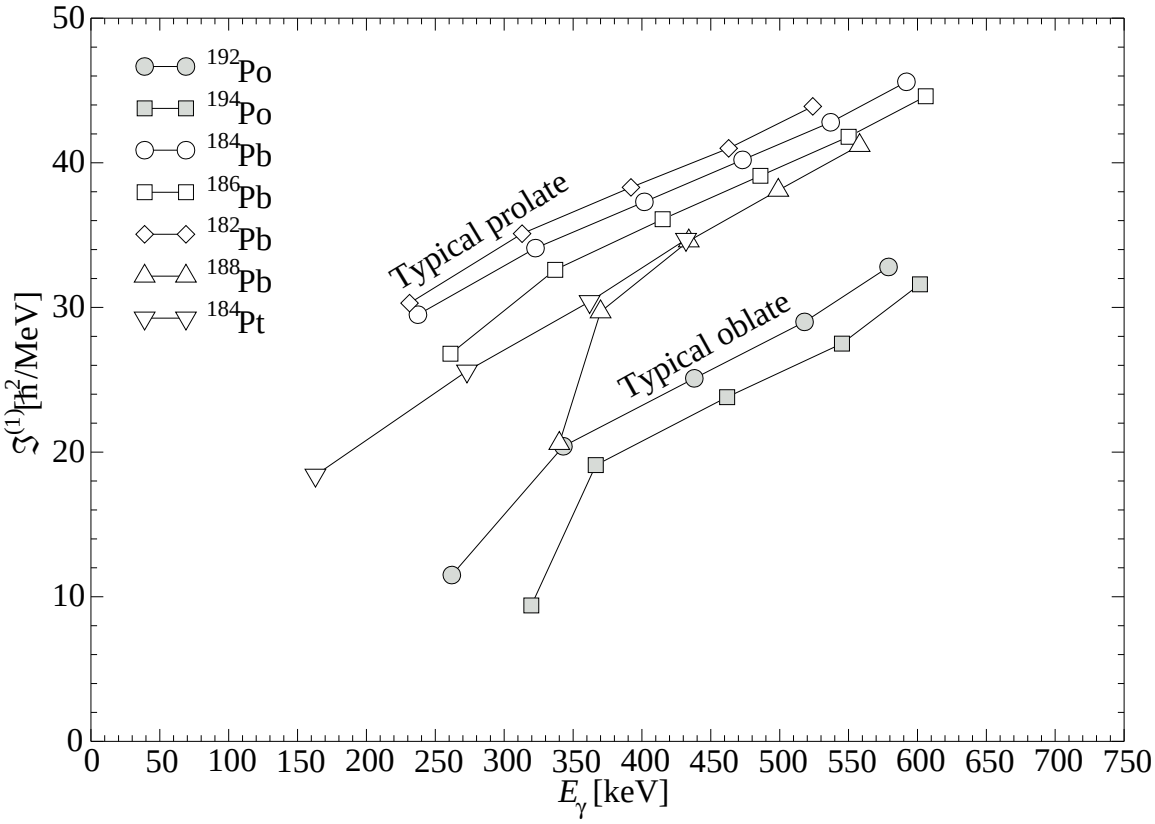

Figure 4.10: Kinematic moments of inertia $\mathcal{J}^{(1)}$ as a function of γ-ray energy E_γ for the typical prolate and oblate bands in the vicinity of neutron-deficient Pb and Po nuclei. The data are adopted from references [Hela 96, Hela 99, Jenk 00, Cock 98, Paka 05b, Garg 86]

state in ^{188}Pb is reflected as a $|Q_t|$ value lower than for higher spin states having pure prolate character. The same effect can also be seen as a drop of the moment of inertia deduced from the 340 keV $4^+ \rightarrow 2^+$ transition in ^{188}Pb. The maximum $|Q_t|$ value is reached already for the $4^+ \rightarrow 2^+$ transition in ^{186}Pb, whereas in ^{188}Pb for the $6^+ \rightarrow 4^+$ transition. Based on these observations the deformation for the prolate band in light Pb isotopes can be deduced using Eq. 2.7 as an average deformation of 4^+, 6^+ and 8^+ states in ^{186}Pb and 6^+ and 8^+ states in ^{188}Pb being $\beta_2 = 0.29(5)$. This value is in agreement with the theoretical values obtained using different approaches [Naza 93, Niks 02, Egid 04, Bend 04].

Bender *et. al.* [Bend 04, Bend 05] have carried out configuration mixing calculations of angular-momentum projected mean-field states using the Skyrme interaction to study the structure and transition probabilities in light Pb isotopes. In that work the transitional quadrupole deformation parameter $\beta_2^{(t)}$ is determined for different configurations in light Pb isotopes. As pointed out in Ref. [Bend 05], $\beta_2^{(t)}$ is comparable to the spectroscopic quadrupole deformation parameter β_2 extracted in this work. A

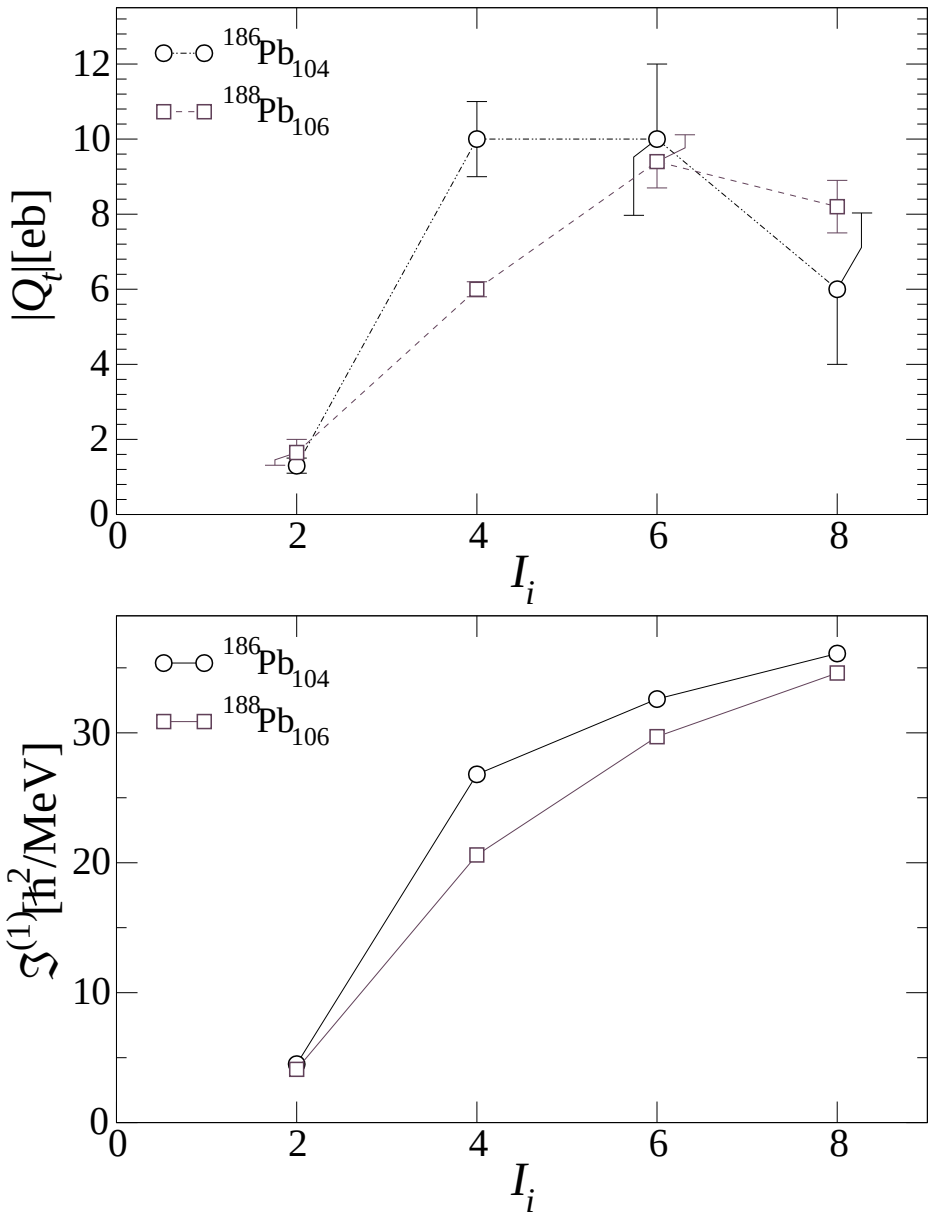

Figure 4.11: Measured $|Q_t|$ values (upper panel) and the moments of inertia (lower panel) for ^{186}Pb and ^{188}Pb.

comparison of calculated $\beta_2^{(t)}$ values to the measured β_2 values is presented in Fig. 4.12. For ^{186}Pb the $\beta_2^{(t)}$ values for $2^+ \rightarrow 0^+$ and $4^+ \rightarrow 2^+$ transitions are given and for in-band transitions between higher lying states $\beta_2^{(t)}$ values are assumed to be similar to that obtained for the $4^+ \rightarrow 2^+$ transition [Bend 04]. The experimental values are reproduced quite well, except for the $4^+ \rightarrow 2^+$ transition in ^{188}Pb and for the $8^+ \rightarrow 6^+$ transition in ^{186}Pb. The overestimated $\beta_2^{(t)}$ value for the $4^+ \rightarrow 2^+$ transition in ^{188}Pb

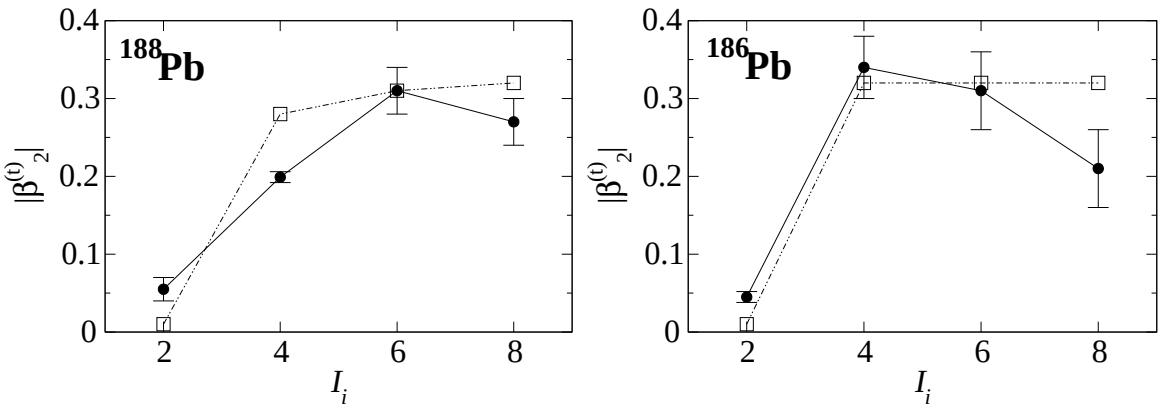

Figure 4.12: A comparison of calculated (open squares) [Bend 04, Bend 05] and measured (filled circles) quadrupole deformation parameters in ^{188}Pb and ^{186}Pb. For the both nuclei calculated $\beta_2^{(t)}$ values within the prolate band for the 4^+, 6^+ and 8^+ states are chosen whereas for the 2^+ states out-of-band transition to the spherical ground state is chosen.

reflects the fact that the calculation underestimates the configuration mixing of the 2^+ state.

The discrepancy between the measured and calculated values for the $8^+ \rightarrow 6^+$ transition in ^{186}Pb could suggest some change in the intrinsic configuration within the band. The $|Q_t|$ values extracted for this transition seem to indicate a drop of collectivity. However, taking into account the error bars the collectivity may well stay at the level of that for the $6^+ \rightarrow 4^+$ transition as expected on the basis of the smooth behaviour of the moments of inertia. On the other hand, if this drop of collectivity is accepted it might be an indication of more complex structural effects dominating at higher spins in ^{186}Pb.

In Ref. [Bend 04] the $B(E2)$ values for the $2^+ \rightarrow 0^+$ and $4^+ \rightarrow 2^+$ transitions de-exciting the prolate as well as oblate 2^+ and 4^+ states in ^{188}Pb are also given. These values are listed in Table 4.10. The measured $B(E2)$ value for $4^+ \rightarrow 2^+$ transition falls between the values calculated for the prolate and oblate configurations, being slightly closer the oblate ones. Also the measured $B(E2)$ value for $2^+ \rightarrow 0^+$ being closer to the calculated oblate to spherical $B(E2)$ would suggest the slightly larger oblate amplitude of the 2^+ state. This is exactly what have been deduced above using the simple two-band mixing model. Unfortunately, calculated prolate to oblate $B(E2)$ value for $4^+ \rightarrow 2^+$ transition is not available in Ref. [Bend 04] for comparison.

Similar angular-momentum projected configuration mixing calculations of mean-field states using the Gogny interaction have been carried out by Rodríguez-Guzmán *et. al.* [Rodr 04] for even-mass $^{182-192}$Pb isotopes. The results are very similar to those obtained by Bender *et. al.* [Bend 04]. The lowest 2^+ state in ^{188}Pb has been predicted

Table 4.10: Comparison of the measured and calculated $B(E2)$ values in ^{188}Pb expressed in W.u. The work of Bender *et. al.* and Rodríguez-Guzmán *et. al.* have been adopted from references [Bend 04] and [Rodr 04], respectively. Calculated in-band $B(E2)$ values are given for both prolate and oblate bands as well as the out-of-band $B(E2)$ values from both deformed configurations to the spherical ground state (Bender *et. al.* and Rodríguez-Guzmán *et. al.*).

I_i^π	this work	Bender *et. al.*		Rodríguez-Guzmán *et. al.*	
		prol. → sph.	obl. → sph.	prol. → sph.	obl. → sph.
2^+	12 - 5	0.2	17.0	1.4	8.7
		prol. → prol.	obl. → obl.	prol. → prol.	obl. → obl.
4^+	160(10)	288	126	262	142

Table 4.11: Comparison of measured and calculated $B(E2)$ values in ^{188}Pb expressed in W.u. The $B(E2)$ values based on the IBM calculations of Hellemans *et. al.* have been adopted from Ref. [Hell 05].

I_i^π	this work	Hellemans *et. al.*
2^+	12 - 5	3
4^+	160(10)	152
6^+	440(70)	197
8^+	350(60)	215

to be a strong admixture of the prolate and oblate shapes, whereas the corresponding state in ^{186}Pb is a rather pure prolate state. Calculated $B(E2)$ values for ^{188}Pb from Ref. [Rodr 04] are listed in Table 4.10. Again, the mixing of the 2^+ state is probably underestimated since the prolate → prolate $B(E2)$ value for the $4^+ \rightarrow 2^+$ transition is too high. This can also be seen as an evidence of the dominant oblate character of the 2^+ state in ^{188}Pb.

In addition to the calculations based on the mean-field, the Interacting Boson Model (IBM) calculations have been carried out for ^{188}Pb by Hellemans *et. al.* [Hell 05] (Table 4.11). These calculations reproduce the values for the two lowest transitions quite well but underestimate the level of collectivity obtained for the 6^+ and 8^+ states. In calculations of Ref. [Hell 05] the IBM parameters for Pb isotopes determined in [Foss 03] were used which, in turn, were obtained from the neighbouring nuclei based on the intruder spin (I_{intr}) arguments [Heyd 92]. It is worthwhile to note that at the time of calculations in References [Hell 05, Bend 04, Rodr 04] only the experimental $B(E2)$ values for the 2^+ and 4^+ states in ^{188}Pb [Dewa 03] were known.

4.4.2 Collective oblate yrast band in ^{194}Po

As already stated in Section 2.4 the yrast band of ^{194}Po is assumed to be deformed having an oblate shape. Especially in ^{192,194}Po the level patterns are close to the adjacent odd-mass nuclei. This indicates a weak coupling of the $i_{13/2}$ neutron to the even-mass core. This could be regarded as a coupling of the odd $i_{13/2}$ neutron to a vibrating core [Foti 97]. With the rotational intruder picture this could be seen as a decoupling of an $i_{13/2}$ neutron hole (low Ω) from an oblate core [Hela 99]. This fact, in addition to the observed kinematic moments of inertia being significantly smaller than those for the prolate shape, suggests an oblate shape for the yrast band in ^{194}Po. In earlier mixing calculations based on the measured level energies [Hela 99] and α-decay hindrance factors [Bijn 95], the yrast 2^+ and 4^+ states in ^{194}Po are interpreted as pure $\pi(4p-2h)$ oblate states, while the ground state is predicted to be strongly mixed.

The measured $|Q_t|$ values of ^{194}Po, ^{186}Pb and ^{188}Pb are plotted in Fig. 4.13 along with the kinematic moments of inertia for the yrast bands in these nuclei. For ^{194}Po the present results reveal that the collectivity of the $2^+ \rightarrow 0^+$ and $4^+ \rightarrow 2^+$ transitions is much lower than for the transitions between the prolate states in ^{186}Pb and ^{188}Pb. This is what is expected for the oblate states, the $|Q_t|$ and β_2 values are lower than those for the prolate states. In the work of Hellemans *et al.* [Hell 05] a comparison of $B(E2)$ values of prolate and oblate bands in ^{188}Pb is presented. This shows remarkably lower $B(E2)$ values for the transitions between the oblate states than between the prolate ones. By using various theoretical frameworks the quadrupole deformation parameter for the oblate shape in ^{194}Po has been predicted to be $\beta_2 \approx 0.2$ [May 77, Oros 99]. In the present work, the corresponding value $\beta_2 = 0.17(3)$ has been extracted as an average of the β_2 values of the yrast 2^+ and 4^+ states.

The similar $|Q_t|$ values for the 2^+ and 4^+ states in ^{194}Po indicates a similar intrinsic structure for both of these states. De Coster *et al.* [De C 99] have carried out IBM calculations for neutron-deficient Po isotopes. Relative $B(E2)$ values in ^{194}Po are obtained in Ref. [De C 99] by carrying out configuration mixing calculation of oblate and near spherical IBM states. Comparison of the calculated relative $B(E2)$ values within the unperturbed bands to the measured $B(E2)$ values suggest rather pure oblate configuration for the ground state and the first 2^+ and 4^+ states in ^{194}Po. The configuration mixing calculation does not reproduce the measured $B(E2)$ values while the trend of the relative $B(E2)$ values between the pure oblate 0^+, 2^+ and 4^+ states is close to what is observed in the present work. Although the near spherical shape mixed with the oblate one in even-mass Po isotopes is not expected to represent such a well-defined energy minimum as the ground state of even-mass Pb isotopes [May 77] the effect of weak mixing of these structures may well fit within the error bars of the measured transition probabilities.

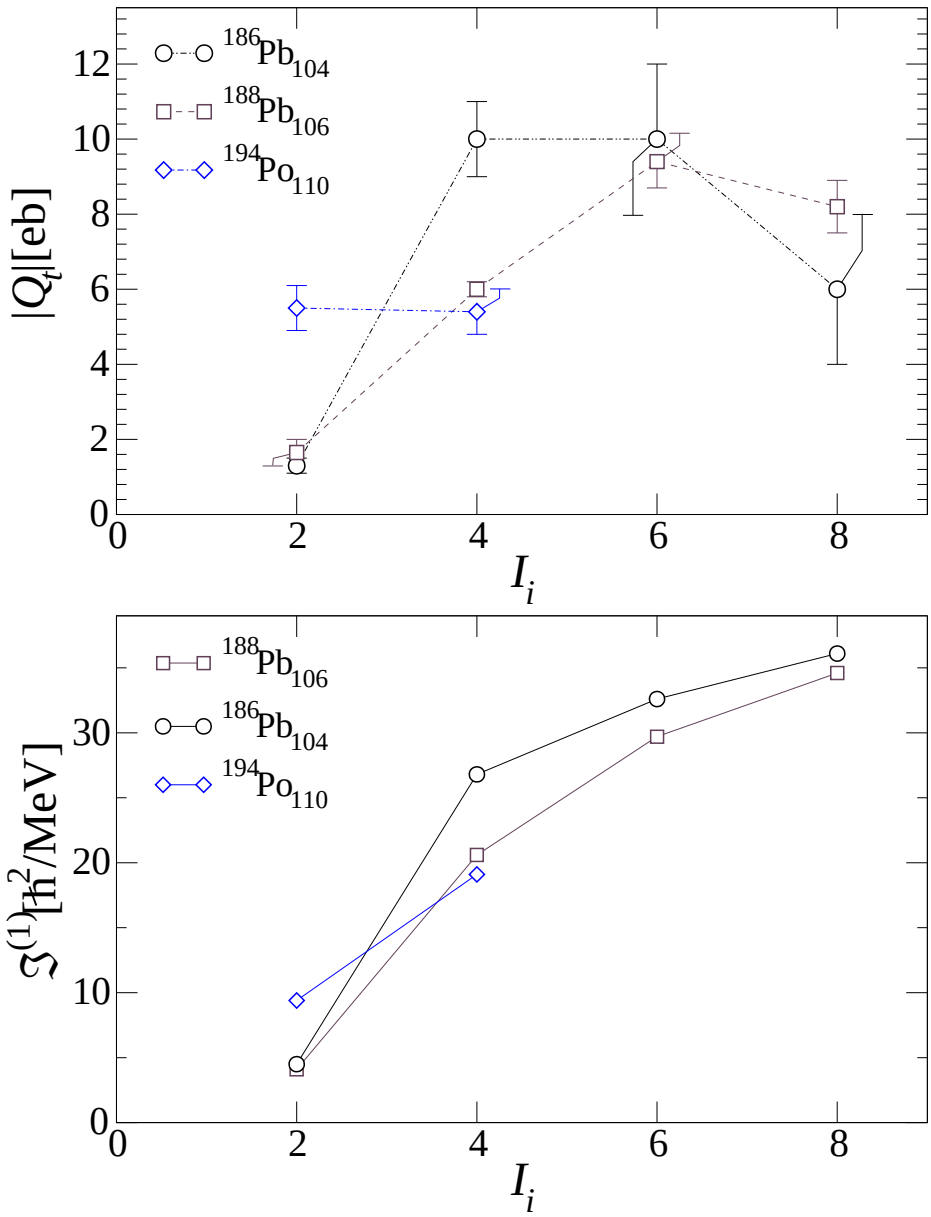

Figure 4.13: Measured $|Q_t|$ values (upper panel) and the moments of inertia (lower panel) for ^{194}Po, ^{186}Pb and ^{188}Pb.

Alternatively, the observed level pattern of ^{194}Po has been interpreted as that for an anharmonic vibrator [Youn 95]. Vibrational systems are characterised by equal energy spacings and nearly degenerate phonon multiplets, $\Delta N_{ph} = \pm 1$ $E2$ selection rules and $B(E2)$ values scaling with the phonon number. Younes and Cizewski [Youn 97] have carried out calculations in the frameworks of Particle Core Model (PCM) and Quasiparticle Random Phase Approximation (QRPA). These calculations based on multiphonon excitations reproduce the level energies quite well but the

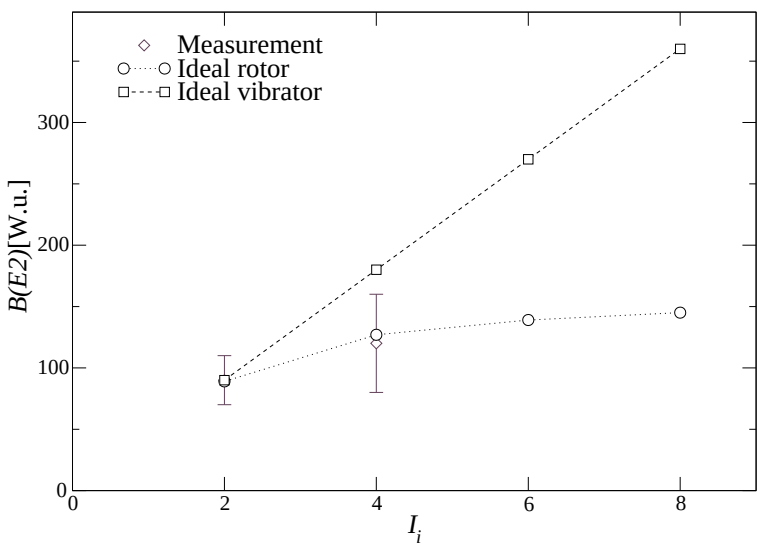

Figure 4.14: $B(E2)$ values for ideal rotor and vibrator as a function of initial spin. Measured values are taken from the present work. Values for the vibrator are calculated using the Eq. 4.1 taking the measured $B(E2; 2_1^+ \rightarrow 0_{g.s.}^+)$ as a starting point. For the rotor, Eq. 2.4 has been used with the value $Q_0 = 5.45$ eb.

value of $B(E2; 2_1^+ \rightarrow 0_{g.s.}^+) = 16.4$ W.u. obtained with QRPA is much lower than that the present experimental value of 90(10) W.u. The effect of intruder structures are not taken into account in PCM and QRPA. This failure of reproducing the measured $B(E2; 2_1^+ \rightarrow 0_{g.s.}^+)$ value indicates the important role of particle-hole intruder structures, enhancing collectivity of the ^{194}Po nucleus. Also Peltonen, Delion and Suhonen [Pelt 05] have calculated α-decay systematics to vibrational 2^+ states using QRPA. In their work a value of 6.8 W.u. for $B(E2; 2_1^+ \rightarrow 0_{g.s.}^+)$ in ^{194}Po has been deduced, which is an order of magnitude smaller than the measured value. Again, in these calculations particle-hole intruder structures were not included.

For a vibrating system, the $B(E2)$ values should follow the relation

$$\sum_{I^f_{N_{ph}-1}} B(E2; I^i_{N_{ph}} \rightarrow I^f_{N_{ph}-1}) = N_{ph} B(E2; 2^+_{1ph} \rightarrow 0^+_{g.s.}), \tag{4.1}$$

where $I^i_{N_{ph}}$ and $I^f_{N_{ph}-1}$ denote the total angular momentum of the initial N phonon and final $N-1$ phonon states, respectively. To illustrate the differences between the rotational and vibrational states in terms of the reduced transition probabilities, $B(E2)$ values for an ideal rotor and vibrator, along with the measured ones are drawn in Fig 4.14. This figure immediately shows the striking difference between the $B(E2)$ values along the band for the vibrating and rotating systems. The measured $B(E2)$ values of ^{194}Po slightly favour the interpretation of the rotating nucleus, but has to be further confirmed by measuring the $B(E2)$ values for the higher spin states. Additionally, one should bear in mind that the proposed anharmonicities of Ref. [Youn 95] would modify the behaviour of the $B(E2)$ values of the vibrator shown in Fig. 4.14.

4.4.3 Comparison of the measured deformation parameters

Prolate yrast bands with kinematic moments of inertia very similar to the prolate bands of ^{186}Pb and ^{188}Pb have been observed in even-mass Hg and Pt nuclei near the $N = 104$ mid-shell. Lifetime measurements of yrast levels have been carried out for ^{184}Hg [Ma 86], ^{186}Hg [Proe 74], ^{184}Pt [Garg 86] and ^{192}Pt [John 77]. A selection of β_2 values extracted from the measured lifetimes are shown in Fig. 4.15. In ^{184}Hg and ^{186}Hg the coexisting weakly deformed oblate ($|\beta_2| \approx 0.15$) and higher deformed prolate ($|\beta_2| \approx 0.28$) bands maintain their purity of structure until they cross at the 4^+ state. The ground state and the first excited 2^+ state are assumed to represent an oblate shape while for the states with higher spin a prolate shape is assumed. This can be seen from Fig. 4.15 where the $|\beta_2|$ values for the 2^+ and 4^+ states in ^{186}Hg lie remarkably lower than those for the prolate states in ^{186,188}Pb measured in this work. The $|\beta_2|$ values for the 6^+ and 8^+ states are within the error bars of corresponding values in ^{186,188}Pb representing similar intruder structures. Also alike kinematic moments of inertia suggests similar intrinsic structure for these nuclei.

In ^{184}Pt the yrast band has been assigned as prolate deformed intruder band with a $\pi(6p - 2h)$ configuration. According to the intruder spin classification, this structure belongs to the same intruder spin multiplet $I_{intr} = 2$ as the prolate $\pi(4p - 4h)$ states in ^{186,188}Pb and thus should have similar band structure (see e.g. Ref. [De C 97]). As seen from Fig. 4.15 the kinematic moments of inertia are very similar for these nuclei. However, the $|\beta_2|$ values for the prolate band in ^{184}Pt are remarkably smaller than those for the prolate states in ^{186,188}Pb. As discussed in Ref. [Garg 86] the mixing of the states plays a crucial role at low spins in ^{184}Pt. States with $I^\pi \geq 6^+$ are considered to be fully unmixed in ^{184}Pt. This, in turn, could lower the $|\beta_2|$ values at low spins compared to those in ^{186,188}Pb. The $|\beta_2|$ value for the 8^+ state in ^{184}Pt fits already well within the error bars of the corresponding values of the other nuclei presented in Fig. 4.15.

As mentioned earlier, taking into account the error bars, the collectivity of the $8^+ \rightarrow 6^+$ transition in ^{186}Pb may well stay at the level of that for the $6^+ \rightarrow 4^+$ transition. But if this lowering of the collectivity is accepted it might indicate some more complex structural effect. Figure 4.15 shows that a slight drop of collectivity is also observed in ^{188}Pb and ^{186}Hg but also these nuclei maintain, within the error bars, their constant $|\beta_2|$ value between the pure deformed states.

The ground state and the lowest 2^+ state in ^{184,186}Hg are assumed to represent a weakly deformed oblate shape with a $\pi(0p - 2h)$ configuration. The present measurements reveal that the collectivity associated with these states are lower than that for the oblate states in ^{194}Po studied in this work. This can be seen from Fig. 4.16 where the $|\beta_2|$ values and the kinematic moments of inertia are plotted for the ^{194}Po, ^{186}Hg and ^{192}Pt. The $|\beta_2|$ values for ^{194}Po lie higher than those for the assumed oblate states in

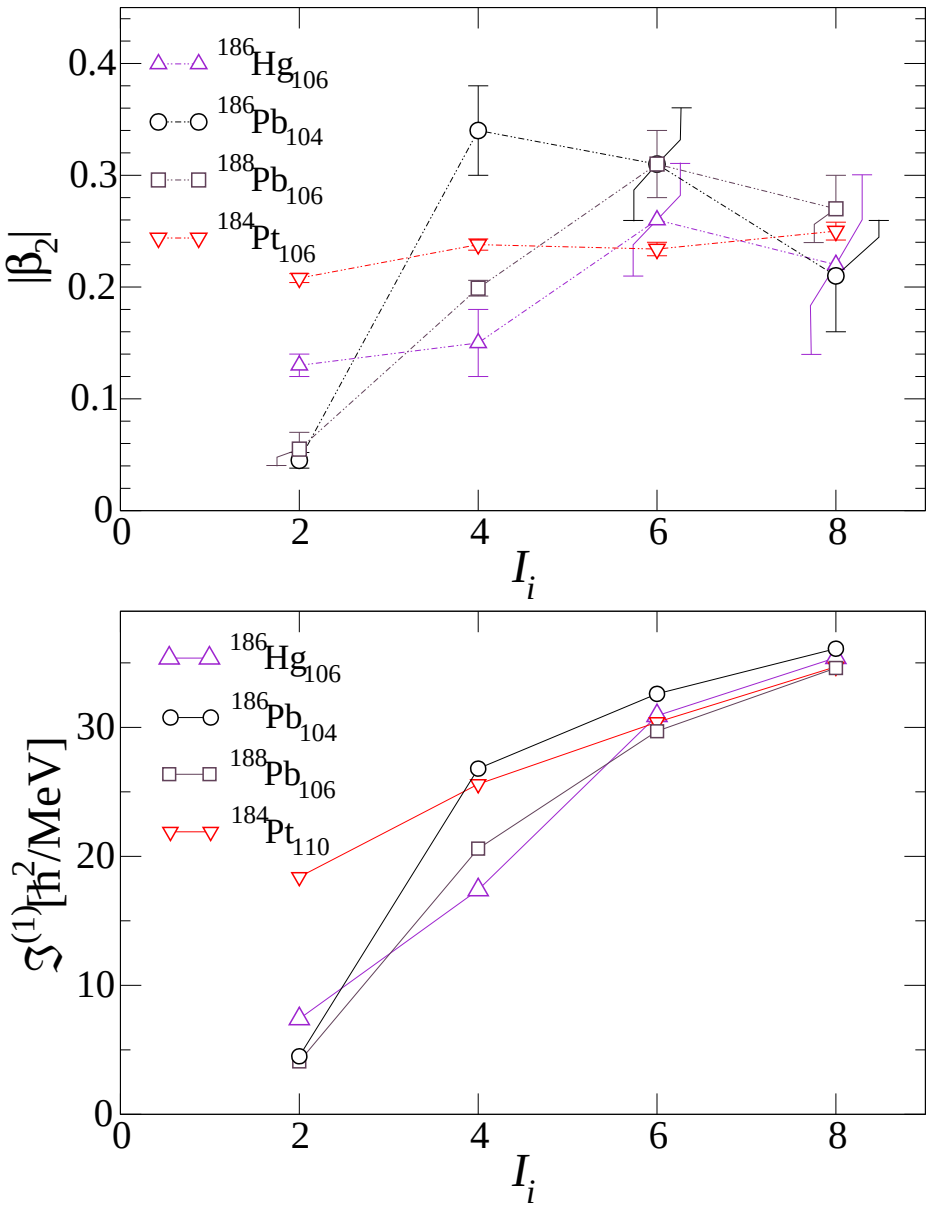

Figure 4.15: Comparison of the measured quadrupole deformation parameters in the vicinity of neutron-deficient Pb nuclei. The data are extracted from references [Proe 74, Garg 86] and from the present work. In the lower panel corresponding kinematic moments of inertia are shown.

^{186}Hg. The lower collectivity associated with oblate states in ^{186}Hg compared to those in ^{194}Po is obvious since the $\pi(4p-2h)$ configuration in ^{194}Po has a larger number of valence quasi-particles than the $\pi(0p-2h)$ configuration in ^{184,186}Hg.

The yrast band in ^{192}Pt has been assigned with the $\pi(0p-4h)$ configuration having a slightly deformed oblate shape. The $|\beta_2|$ values for the yrast states in ^{192}Pt extracted

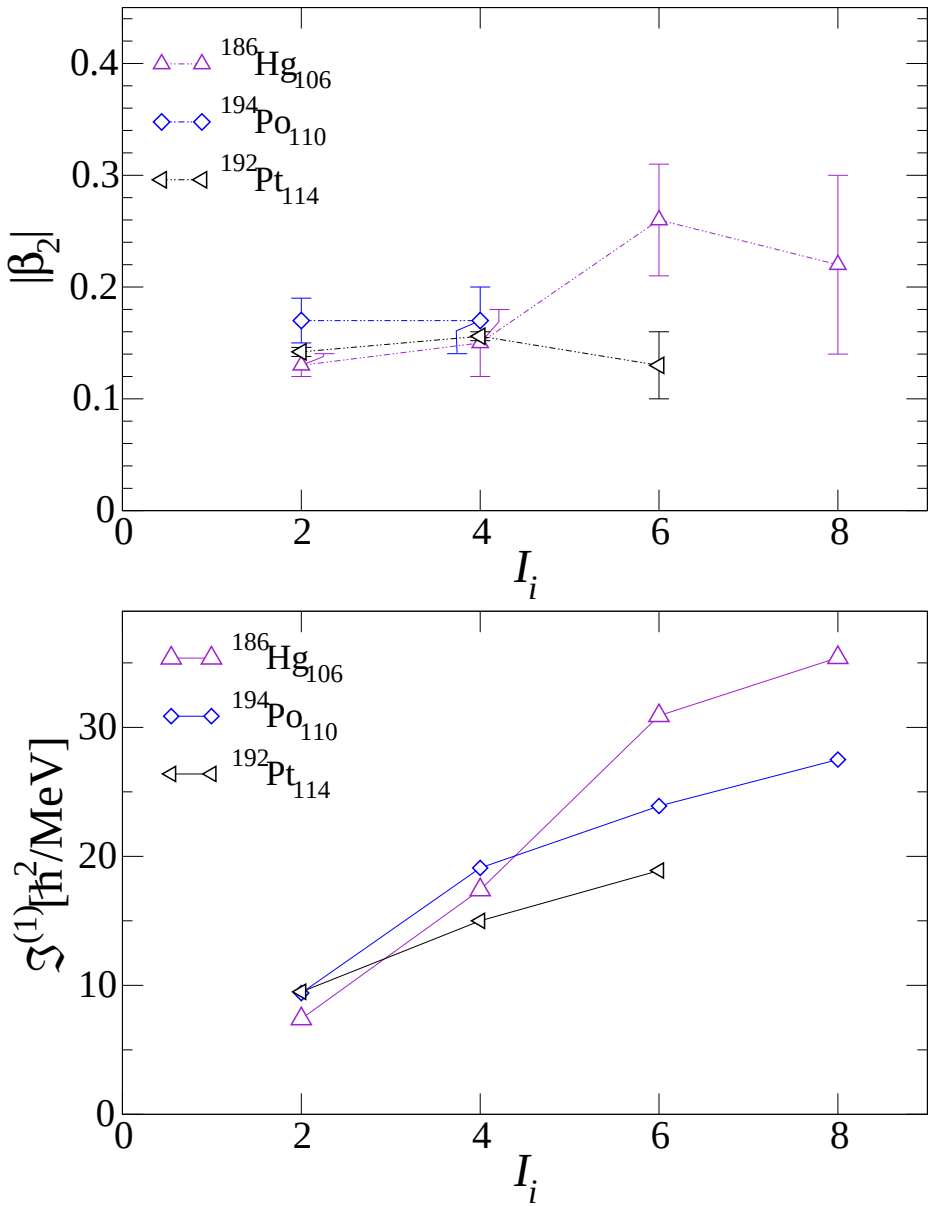

Figure 4.16: Comparison of the measured quadrupole deformation parameters in the vicinity of neutron-deficient Po nuclei. The data are extracted from references [Proe 74, John 77] and from the present work. In the lower panel corresponding kinematic moments of inertia are drawn.

from the measurements in Ref. [John 77] have been plotted in Fig. 4.16. The deformation of the yrast states in ^{192}Pt is slightly smaller than that for ^{194}Po. The lower collectivity of the yrast states in ^{192}Pt compared to the ones in ^{194}Po is indicated by the measured $B(E2)$ values. The $B(E2)$ value of the $2^+ \rightarrow 0^+$ transition in ^{192}Pt (52(3) W.u. [John 77]) is approximately a half of what is measured in the present work for ^{194}Po. This is also observed as higher kinematic moments of inertia of the

yrast states in ^{194}Po (Fig. 4.16).

Compared to the well understood doubly magic spherical nucleus ^{208}Pb from where the electromagnetic features of the spherical states in Pb nuclei can be extracted, little is known about the corresponding near spherical states in Po nuclei. Further lifetime measurements of heavier Po isotopes, where the intruder structures lie higher in energy, would be required to study the degree of collectivity and configuration mixing as a function of neutron number and angular momentum and thus obtain information about the electromagnetic properties of the near spherical states in neutron-deficient Po nuclei.

5 Summary

RDDS lifetime measurements of yrast states in ^{186,188}Pb and ^{194}Po have been carried out at the Accelerator Laboratory of the University of Jyväskylä. The Köln plunger device was installed at the JUROGAM target position and coupled to the RITU gas-filled separator. With this set-up the recoiling evaporation residues were separated from the background introduced by other unwanted nuclear reactions and identified by the GREAT spectrometer at the focal plane of RITU. As the pioneering experiments carried out in this work demonstrate, the RDT technique provides essentially background free γ-ray spectra for lifetime measurements and enables the extension of the RDDS studies to exotic nuclei near the proton drip-line with relatively low cross-sections.

In this study the quadrupole deformation parameter $|\beta_2|$ has been extracted for both prolate and oblate shapes in the vicinity of neutron-deficient Pb nuclei having the values of $|\beta_2| = 0.29(5)$ (^{186,188}Pb) and $|\beta_2| = 0.17(3)$ (^{194}Po), respectively. The co-existing shapes lying low in excitation energy are characteristic of neutron-deficient Pb region nuclei and therefore offer the ultimate laboratory for nuclear structure studies. This, in addition to the measured values of reduced transition probabilities $B(E2)$, has confirmed the collective behaviour of excited states in this region. The electromagnetic properties of prolate bands have been probed in ^{186,188}Pb, while the proposed oblate band in ^{186,188}Pb is non-yrast and therefore too weakly populated by fusion-evaporation reactions for RDDS studies. Electromagnetic properties of the oblate yrast band in ^{194}Po have been measured completing the study of deformed structures in the neutron-deficient Pb and Po nuclei.

By means of lifetime measurements direct information about the configuration mixing can be deduced. For the 2^+ state in ^{188}Pb the $|Q_t|$ value indicates that the mixing of the oblate and prolate shapes plays a crucial role, while in ^{186}Pb the corresponding state is already a pure member of the prolate band. A comparison of the present results of ^{186,188}Pb to the earlier lifetime measurements of prolate states near $Z = 82$ and $N = 104$ shows that within the error bars the level of collectivity of these states is similar. A lot of theoretical effort has been put towards investigating the structure of neutron-deficient Pb isotopes. These calculations have usually reproduced the energy levels and so far known $B(E2)$ values reasonably well, but the results provided by the present study gain experimental input for the theoretical models and sets stringent conditions for more precise calculations.

In contrast to the earlier predictions, the present work indicates that the ground state state in ^{194}Po is dominantly oblate in character. This can be seen from the nearly constant $|Q_t|$ values of the ground state and the first excited 2^+ state. The availability of the calculated $B(E2)$ values of the yrast band in ^{194}Po is rather limited. The existing values for the $2^+ \rightarrow 0^+$ transition are underestimated roughly by a factor of two. To further study the collectivity in neutron-deficient Po nuclei, the lifetime measurements of the heavier isotopes, where the intruder structures lie higher in energy, would be required.

So far, the RDT measurements with stable beams are the most efficient way to study neutron-deficient nuclei near $Z = 82$. Lifetime measurements can be carried out employing the RDDS method, which is so far the only feasible method to gather lifetime information in such exotic nuclei as described in this work. However, the continuous technical development of radioactive ion beams has recently reached new goals and hopefully in the future radioactive ion beam facilities will provide such exotic beams as ^{186}Pb with a high beam quality. This would open up new possibilities, e.g. to measure $B(E2)$ values via Coulomb excitation. With this technique states other than yrast ones are also accessible for lifetime studies.

Combining the high selectivity of tagging techniques with the RDDS method provides important technical development concerning the future Ge-detector arrays instrumented with digital electronics (e.g. AGATA). Also the employment of the RDDS method with radioactive ion beams is in progress and gains knowledge from the RDDS measurements of very exotic species carried out with stable beams.

Shape coexistence in the vicinity of neutron-deficient $Z = 82$ nuclei is a topic of strong current interest. In order to further elucidate the origin of this phenomenon lifetimes of the low-lying 0^+ excited states would be required. Due to the $E0$ character of these $0^+_{2,3} \rightarrow 0^+_{g.s.}$ transition this would require conversion electron measurements. So called recoil shadow conversion electron measurements are planned to be carried out to obtain the lifetime information of the excited 0^+ states in ^{186}Pb and ^{194}Po.

To conclude, the continuously evolving understanding of the nuclear structure of the neutron-deficient Pb and Po nuclei will allow the gain of important information and input for theoretical calculations from the lifetime measurements such as the ones described in the present work.

References

[Albe 91] D. Alber, R. Alfier, C. E. Bach, D. B. Fossan, H. Grawe, H. Kluge, M. Lach, K. H. Maier, M. Schramm, R. Schubart, M. P. Waring, L. Wood, H. Hübel, and Jing-ye Zhang. *Zeitschrift für Physik A*, Vol. 339, p. 225, 1991.

[Alla 98] R. G. Allat, R. D. Page, M. Leino, T. Enqvist, K. Eskola, P. T. Greenlees, P. Jones, R. Julin, P. Kuusiniemi, W. H. Trzaska, and J. Uusitalo. *Physics Letters B*, Vol. 437, p. 29, 1998.

[Alva 93] C. R. Alvarez. *Nuclear Physics News*, Vol. 3, No. 3, 1993.

[Andr 00] A. N. Andreyev, M. Huyse, P. Van Duppen, L. Weissman, D. Ackermann, J. Gerl, F. P. Heßberger, S. Hofmann, A. Kleinböhl, G. Münzenberg, S. Reshitko, C. Schlegel, H. Schaffner, P. Cagarda, M. Matos, S. Saro, A. Keenan, C. Moore, C. D. O'Leary, R. D. Page, M. Taylor, H. Kettunen, M. Leino, A. Lavrentiev, R. Wyss, and K. Heyde. *Nature (London)*, Vol. 405, p. 430, 2000.

[Andr 99a] A. N. Andreyev, D. Ackermann, P. Cagarda, J. Gerl, F. Hessberger, S. Hofmann, M. Huyse, A. Keenan, H. Kettunen, A. Kleinbohl, A. Lavrentiev, M. Leino, B. Lommel, M. Matos, G. Münzenberg, C. Moore, C. D. O'Leary, R. D. Page, S. Reshitko, S. Saro, C. Schlegel, H. Schaffner, M. Taylor, P. Van Duppen, L. Weissman, and R. Wyss. *European Physical Journal A*, Vol. 6, p. 381, 1999.

[Andr 99b] A. N. Andreyev, N. Bijnens, M. Huyse, P. Van Duppen, M. Leino, T. Enqvist, P. Kuusiniemi, W. Trzaska, J. Uusitalo, N. Fotiades, J. A. Cizewski, D. P. McNabb, K. Y. Ding, C. N. Davids, R. V. F. Janssens, D. Seweryniak, M. P. Carpenter, H. Amro, P. Decrock, P. Reiter, D. Nisius, L. T. Brown, S. Fischer, T. Lauritsen, J. Wauters, C. R. Bingham, and L. F. Conticchio. *Journal of Physics G*, Vol. 25, p. 835, 1999.

[Baxt 93] A. M. Baxter, A. P. Byrne, G. D. Dracoulis, R. V. F. Janssens, I. G. Bearden, R. G. Henry, D. Nisius, C. N. Davids, T. L. Khoo, T. Lauritsen, H. Penttilä, D. J. Henderson, and M. P. Carpenter. *Physical Review C*, Vol. 48, p. R2140, 1993.

[Beau 92] C. W. Beausang, S. A. Forbes, P. Fallon, P. J. Nolan, P. J. Twin, J. N. Mo, J. C. Lisle, M. A. Bentley, J. Simpson, F. A. Beck, D. Curien, G. deFrance, G. Duchêne, and D. Popescu. *Nuclear Instruments and Methods in Physics Research A*, Vol. 313, p. 37, 1992.

[Bend 04] M. Bender, P. Bonche, T. Duguet, and P.-H. Heenen. *Physical Review C*, Vol. 69, p. 064303, 2004.

[Bend 05] M. Bender and P.-H. Heenen. *Journal of Physics G*, Vol. 31, p. S1367, 2005.

[Bern 95] L. A. Bernstein, J. A. Cizewski, H.-Q. Jin, W. Younes, R. G. Henry, L. P. Farris, A. Charos, M. P. Carpenter, R. V. F. Janssens, T. L. Khoo, T. Lauritsen, I. G. Bearden, D. Ye, J. A. Becker, E. A. Henry, M. J. Brinkman, J. R. Hughes, A. Kuhnert, T. F. Wang, M. A. Stoyer, R. M. Diamond, F. M. A. Deleplngue, A. O. Macchiavelli, I. Y. Lee, B. Cederwall, J. R. B. Oliveira, J. Burde, P. Fallon, C. Duyar, J. E. Draper, E. Rubel, and D. T. Vo. *Physical Review C*, Vol. 52, p. 621, 1995.

[Bijn 95] N. Bijnens, P. Decrock, S. Franchoo, M. Gaelens, M. Huyse, H.-Y. Hwang, I. Reusen, J. Szerypo, J. G. Correia, A. Jokinen, P. Van Duppen, and The ISOLDE collaboration. *Physical Review Letters*, Vol. 75, p. 4571, 1995.

[Bijn 98] N. Bijnens, P. Decrock, S. Franchoo, M. Gaelens, M. Huyse, H.-Y. Hwang, I. Reusen, J. Szerypo, J. von Schwarzenberg, G. Vancraeynest, P. Van Duppen, and J. Wauters. *Physical Review C*, Vol. 58, p. 754, 1998.

[Bohr 75] A. Bohr and B. M. Mottelsson. *Nuclear Structure, Vol. 2*. W. A. Benjamin Inc., Massachusetts, USA, 1975.

[Cock 98] J. F. C. Cocks, M. Muikkku, W. Korten, R. Wadsworth, S. Chmel, J. Domscheit, P. T. Greenlees, K. Helariutta, I. Hibbert, M. Houry, D. Jenkins, P. Jones, R. Julin, S. Juutinen, H. Kankaanpää, H. Kettunen, P. Kuusiniemi, M. Leino, Y. Le Coz, R. Lucas, E. Mergel, R. D. Page, A. Savelius, and W. Trzaska. *European Physical Journal A*, Vol. 3, p. 17, 1998.

[De C 00] C. De Coster, B. Decroix, and K. Heyde. *Physical Review C*, Vol. 61, p. 067306, 2000.

[De C 97] C. De Coster, B. Decroix, K. Heyde, J. L. Wood, J. Jolie, and H. Lehmann. *Nuclear Physics A*, Vol. 621, p. 802, 1997.

[De C 99] C. De Coster, B. Decroix, K. Heyde, J. Jolie, H. Lehmann, and J. L. Wood. *Nuclear Physics A*, Vol. 651, p. 31, 1999.

[Dewa 03] A. Dewald, R. Peusquens, B. Saha, P. von Brentano, A. Fitzler, T. Klug, I. Wiederhöver, M. P. Carpenter, A. Heinz, R. V. F. Janssens, F. G. Kondev, C. J. Lister, D. Seweryniak, K. Abu Saleem, R. K. J. R. Cooper, C. J. Barton, K. Zyromski, C. W. Beausang, Z. Whang, P. Petkov, A. M. Oros-Peusquens, U. Garg, and S. Zhu. *Physical Review C*, Vol. 68, p. 034314, 2003.

[Dewa 06] A. Dewald. Private communications, 2006.

[Dewa 89] A. Dewald, S. Harissopoulos, and P. von Brentano. *Zeitschrift für Physik A*, Vol. 334, p. 163, 1989.

[Drac 03] G. D. Dracoulis, G. J. Lane, A. M. Baxter, T. Kibédi, A. O. Macchiavelli, and P. F. amd R. M. Clark. *Physical Review C*, Vol. 67, p. 051301(R), 2003.

[Drac 04] G. D. Dracoulis, G. J. Lane, A. P. Byrne, T. Kibédi, A. M. Baxter, A. O. Macchiavèlli, P. Fallon, and R. M. Clark. *Physical Review C*, Vol. 69, p. 054318, 2004.

[Drac 94] G. D. Dracoulis. *Physical Review C*, Vol. 49, p. 3324, 1994.

[Drac 98] G. D. Dracoulis, A. P. Byrne, and A. M. Baxter. *Physics Letters B*, Vol. 432, p. 37, 1998.

[Egid 04] J. L. Egido, L. M. Robledo, and R. R. Rodríguez-Guzmán. *Physical Review Letters*, Vol. 93, p. 082502, 2004.

[Fant 90] B. Fant, T. Weckström, and A. Källberg. *Physica Scripta*, Vol. 41, p. 652, 1990.

[Fant 91] B. Fant, R. J. Tanner, P. A. Butler, A. N. James, G. D. Jones, R. J. Poynter, C. A. White, K. L. Ying, D. J. G. Love, J. Simpson, and K. A. Connell. *Journal of Physics G*, Vol. 17, p. 319, 1991.

[Foss 03] R. Fossion, K. Heyde, G. Thiamova, and P. Van Isacker. *Physical Review C*, Vol. 67, p. 024306, 2003.

[Foti 97] N. Fotiades, J. A. Cizewski, D. P. McNabb, K. Y. Ding, C. N. Davids, R. V. F. Janssens, D. Seweryniak, M. P. Carpenter, H. Amro, P. Decrock, P. Reiter, D. Nisius, L. T. B. S. Fischer, T. Lauritsen, J. Wauters, C. R. Bingham, M. Huyse, A. Andreyev, and L. F. Conticchio. *Physical Review C*, Vol. 56, p. 723, 1997.

[Garg 86] U. Garg, A. Chaudhury, M. W. Drigert, E. G. Funk, J. W. Mihelich, D. C. Radford, H. Helppi, R. Holzmann, R. V. F. Janssens, T. L. Khoo, A. M. Van Den Berg, and J. L. Wood. *Physics Letters B*, Vol. 180, p. 319, 1986.

[Gree 04] P. T. Greenlees, A. N. Andreyev, J. Bastin, F. Becker, E. Bouchez, P. A. Butler, J. F. C. Cocks, Y. Le Coz, K. Eskola, J. Gerl, K. Hauschild, K. Helariutta, R.-D. Hertzberg, F. P. Heßberger, R. D. Humphreys, A. Hürstel, D. G. Jenkins, G. D. Jones, P. Jones, R. Julin, S. Juutinen, H. Kankaanpää, A. Keenan, H. Kettunen, T. L. Khoo, W. Korten, P. Kuusiniemi, M. Leino, A.-P. Leppänen, M. Muikku, P. Nieminen, R. D. Page, T. Page, J. Pakarinen, P. Rahkila, P. Reiter, Ch. Schlengel, C. Scholey, Ch. Theisen, J. Uusitalo, K. Van de Vel, R. Wadsworth, and H. J. Wollersheim. *European Physical Journal A*, Vol. 20, p. 87, 2004.

[Grod 62] L. Grodzins. *Physics Letters*, Vol. 2, p. 88, 1962.

[Hari 87] S. Harissopulos, A. Dewald, A. Gelberg, P. V. Brentano, K. Loewenich, K. Schiffer, and K. O. Zell. *Nuclear Physics*, Vol. A467, p. 528, 1987.

[Hees 93] J. Heese, K. H. Maier, H. Grawe, J. Grebosz, H. Kluge, W. Meczynski, M. Schramm, R. Schubart, K. Spohr, and J. Styczen. *Physics Letters B*, Vol. 302, p. 390, 1993.

[Hela 96] K. Helariutta, T. Enqvist, P. Jones, S. Juutinen, P. Jämsen, H. Kankaanpää, P. Kuusiniemi, M. Leino, M. Muikku, M. Piiparinen, A. Savelius, W. H. Trzaska, S. Törmänen, J. Uusitalo, R. G. Allat, P. A. Butler, P. T. Greenlees, and R. D. Page. *Physical Review C*, Vol. 54, p. R2799, 1996.

[Hela 99] K. Helariutta, J. F. C. Cocks, T. Enqvist, P. T. Greenlees, P. Jones, R. Julin, S. Juutinen, P. Jämsen, H. Kankaanpää, H. Kettunen, P. Kuusiniemi, M. Leino, M. Muikku, M. Piiparinen, P. Rahkila, A. Savelius, W. H. Trzaska, S. Törmänen, J. Uusitalo, R. G. Allat, P. A. Butler, R. D. Page, and M. Kapusta. *European Physical Jourbal A*, Vol. 6, p. 289, 1999.

[Hell 05] V. Hellemans, R. Fossion, S. De Baerdemacker, and K. Heyde. *Physical Review C*, Vol. 71, p. 034308, 2005.

[Heyd 92] K. Heyde, C. De Coster, J. Jolie, and J. L. Wood. *Physical Review C*, Vol. 46, p. 541, 1992.

[Jenk 00] D. G. Jenkins, M. Muikku, P. T. Greenlees, K. Hauschild, K. Helariutta, P. M. Jones, R. Julin, S. Juutinen, H. Kankaanpää, N. S. Kelsall, H. Kettunen, P. Kuusiniemi, M. Leino, C. J. Moore, P. Nieminen, C. D. O'Leary, R. D. Page, P. Rahkila, W. Reviol, M. J. Taylor, J. Uusitalo, and R. Wadsworth. *Physical Review C*, Vol. 62, p. 021302(R), 2000.

[John 77] N. R. Johnson, P. P. Hubert, E. Eichler, D. G. Sarantites, J. Urbon, S. W. Yates, and T. Lindblad. *Physical Review C*, Vol. 15, p. 1325, 1977.

[Jone 69] K. W. Jones, A. Z. Schwarzschildt, E. K. Warburton, and D. B. Fossan. *Physical Review*, Vol. 178, p. 1773, 1969.

[Juli 01] R. Julin, K. Helariutta, and M. Muikku. *Journal of Physics G*, Vol. 27, p. R109, 2001.

[Kant 95] J. Kantele. *Handbook of nuclear spectrometry.* Academic Press Ltd, 1995.

[Laza 01] I. H. Lazarus, D. E. Appelbe, P. A. Butler, P. J. Coleman-Smith, J. R. Creswell, S. J. Freeman, R. D. Herzberg, I. Hibbert, D. T. Joss, S. C. Letts, R. D. Page, V. F. E. Pucknell, P. H. Regan, J. Sampson, J. Simpson, J. Thornhill, and R. Wadsworth. *IEEE Transaction on Nuclear Science*, Vol. 48, No. 3, 2001.

[Lein 95] M. Leino, J. Äystö, T. Enqvist, P. Heikkinen, A. Jokinen, M. Nurmia, A. Ostrovski, W. H. Trzaska, J. Uusitalo, K. Eskola, P. Armbruster, and V. Ninov. *Nuclear Instruments and Methods in Physics Research B*, Vol. 99, p. 653, 1995.

[Ma 86] W. C. Ma, A. V. Ramayya, J. H. Hamilton, S. J. Robinson, J. D. Cole, E. E. H. Spejewski, R. Bengtsson, W. Nazarewicz, and J.-Y. Zhang. *Physics Letters*, Vol. 167B, p. 277, 1986.

[Maj 90] A. Maj, H. Grawe, H. Kluge, A. Kuhnert, K. H. Maier, J. Recht, N. Roy, H. Hübel, and M. Guttormsen. *Nuclear Physics A*, Vol. 509, p. 413, 1990.

[May 77] F. R. May, V. V. Paskevich, and S. Frauendorf. *Physics Letters*, Vol. B 68, p. 113, 1977.

[McDo 78] R. J. McDonald and J. E. Draper. *Physical Review C*, Vol. 17, p. 944, 1978.

[Moor 95] E. F. Moore, M. P. Carpenter, Y. Liang, R. V. F. Janssens, I. Ahmad, I. G. Bearden, P. J. Daly, M. W. Drigert, B. Fornal, U. Garg, Z. W. Grabowski, H. L. Harrington, R. G. Henry, T. L. Khoo, T. Lauritsen, R. H. Mayer, D. Nisius, W. Reviol, and M. Sferrazza. *Physical Review C*, Vol. 51, p. 115, 1995.

[Mori 76] H. Morinaga and T. Yamazaki. *In beam gamma-ray spectroscopy.* North Holland publishing company, 1976.

[Naza 93] W. Nazarewicz. *Physics Letters B*, Vol. 305, p. 195, 1993.

[Niks 02] T. Nikšić, D. Vretenar, P. Ring, and G. A. Lalazissis. *Physical Review C*, Vol. 65, p. 054320, 2002.

[Nola 79] P. J. Nolan and J. F. Sharpey-Shafer. *Reports on Progress in Physics*, Vol. 42, p. 1, 1979.

[Oros 99] A. M. Oros, K. Heyde, C. De Coster, B. Decroix, R. Wyss, B. R. Barret, and P. Navratil. *Nuclear Physics A*, Vol. 645, p. 107, 1999.

[Page 01] R. D. Page, D. Ackermann, A. N. Andreyev, P. Cagarda, K. Eskola, J. Gerl, P. T. Greenlees, F. P. Heßberger, K. Heyde, S. Hoffmann, M. Huyse, P. Jones, D. T. Joss, R. Julin, S. Juutinen, H. Kankaanpää, A. Keenan, H. Kettunen, A. Kleinböhl, P. Kuusiniemi, A. Lavrentiev, M. Leino, M. Matos, A. Melarangi, C. J. P. Moore, M. Muikku, G. Münzenberger, P. Nieminen, C. D. O'Leary, P. Rahkila, S. Reshitko, H. Schaffner, C. Schlegel, C. Scholey, M. J. Taylor, J. Uusitalo, K. Van de Vel, P. Van Duppen, L. Weissman, C. Wheldon, and R. Wyss. In: J. Äystö, P. Dendooven, A. Jokinen, and M. Leino, Eds., *Proceedings of the Third International Conference on Exotic Nuclei and Atomic Masses ENAM2001*, p. 309, Springer-Verlag, Berlin, 2001.

[Page 03] R. Page, A. Andreyev, D. Appelbe, P. Butler, S. Freeman, P. Greenlees, R.-D. Herzberg, D. Jenkins, G. Jones, P. Jones, D. Joss, R. Julin, H. Kettunen, M. Leino, P. Rahkila, P. Reagan, J. Simpson, J. Uusitalo, S. Vincent, and R. Wadsworth. *Nuclear Instruments and Methods in Physics Research B*, Vol. 204, p. 634, 2003.

[Paka 05a] J. Pakarinen. PhD thesis, University of Jyväskylä, 2005.

[Paka 05b] J. Pakarinen, I. G. Darby, S. Eeckhaudt, T. Enqvist, T. Grahn, P. T. Greenlees, V. Hellemans, K. Heyde, F. Johnston-Theasby, P. Jones, R. Julin, S. Juutinen, H. Kettunen, M. Leino, A.-P. Leppänen, P. Nieminen, M. Nyman, R. D. Page, P. M. Raddon, P. Rahkila, S. Scholey, J. Uusitalo, and R. Wadsworth. *Physical Review C*, Vol. 72, p. 011304(R), 2005.

[Paul 95] E. S. Paul, P. J. Woods, T. Davinson, R. D. Page, P. J. Sellin, R. M. C. C. W. Beausang, R. A. Cunningham, S. A. Forbes, D. B. Fossan, A. Gizon, J. Gizon, K. Hauschildt, I. M. Hibbert, A. N. James, D. R. LaFosse, I. Lazarus, H. Schnare, J. Simpson, R. Wadsworth, and M. P. Waring. *Physical Review C*, Vol. 51, p. 78, 1995.

[Pelt 05] S. Peltonen, D. S. Delion, and J. Suhonen. *Physical Review C*, Vol. 71, p. 044315, 2005.

[Penn 87] J. Penninga, W. H. A. Hesselink, A. Balanda, A. Stolk, H. Verheul, J. van Klinken, H. J. Riezebos, and M. J. A. de Voigt. *Nuclear Physics A*, Vol. 471, p. 535, 1987.

[Petk 92] P. Petkov, S. Harissopulos, A. Dewald, M. Stolzenwald, G. Böhm, P. Sala, K. Schiffer, A. Gelberg, and K. O. Zelland P. von Brentano. *Nuclear Physics*, Vol. A543, p. 589, 1992.

[Plom 93] A. J. M. Plompen, M. N. Harakeh, W. H. A. Hesselink, G. van 't Hof, N. Kalantar-Nayestanaki, J. P. S. van Schagen, M. P. Carpenter, I. Ahmad, I. G. Bearden, R. V. F. Janssens, T. L. Khoo, T. Lauritsen, Y. Liang, U. Garg, W. Reviol, and D. Ye. *Nuclear Physics A*, Vol. 562, p. 61, 1993.

[Proe 74] D. Proetel, R. M. Diamond, and F. S. Stephens. *Physics Letters*, Vol. 48B, p. 102, 1974.

[Rahk] P. Rahkila. to be published.

[Rodr 04] R. R. Rodríguez-Guzmán, J. L. Egido, and L. M. Robledo. *Phys. Rev. C*, Vol. 69, p. 054319, 2004.

[Schw 68] A. Z. Schwarzschildt and E. K. Warburton. *Annual Review of Nuclear Science*, Vol. 18, p. 265, 1968.

[Simo 86] R. S. Simon, K.-H. Schmidt, F. P. Heßberger, S. Hlavac, M. Honusek, G. Münzenberger, H.-G. Clerc, U. Gollerthan, and W. Schwab. *Zeitschrift für Physik A*, Vol. 325, p. 197, 1986.

[Sten 85] C. Stenzel, H. Grawe, H.-E. Mahnke, and K. H. Maier. *Zeitschrift für Physik A*, Vol. 322, p. 83, 1985.

[Step 73] F. S. Stephens, R. M. Diamond, and S. G. Nilsson. *Physics Letters*, Vol. 44B, p. 429, 1973.

[Van 03a] K. Van de Vel, A. N. Andreyev, D. Ackermann, H. J. Boardman, P. Cagarda, J. Gerl, F. P. Heßberger, S. Hofmann, M. Huyse, D. Karlgren, I. Kojouharov, M. Leino, B. Lommel, G. Münzenberg, C. Moore, R. D. Page, S. Saro, P. V. Duppen, and R. Wyss. *Physical Review C*, Vol. 68, p. 054311, 2003.

[Van 03b] K. Van de Vel, A. N. Andreyev, R. D. Page, H. Kettunen, P. T. Greenlees, P. Jones, R. Julin, S. Juutinen, H. Kankaanpää, A. Keenan, P. Kuusiniemi, M. Leino, M. Muikku, P. Nieminen, P. R. nad J. Uusitalo, K. Eskola, A. Hürstel, M. Huyse, Y. Le Coz, M. B. Smith, P. Van Duppen, and R. Wyss. *European Physical Journal A*, Vol. 17, p. 167, 2003.

[Van 87] P. Van Duppen, E. Coenen, K. Deneffe, and M. Huyse. *Physical Review C*, Vol. 35, p. 1861, 1987.

[Youn 95] W. Younes, J. A. Cizewski, H.-Q. Jin, L. A. Bernstein, D. P. McNabb, C. N. Davids, R. F. V. Janssens, T. L. Khoo, C. J. Lister, D. J. Blumenthal, M. P. Carpenter, D. Henderson, R. G. Henry, T. Lauritsen, D. T. Nisius, H. T. Penttilä, and M. W. Drigert. *Physical Review C*, Vol. 52, p. R1723, 1995.

[Youn 97] W. Younes and J. A. Cizewski. *Physical Review C*, Vol. 55, p. 1218, 1997.